Unsteady Aerodynamics of Flexible Wings in Transverse Gusts

Fidel Fernandez, David Cleaver, and Ismet Gursul
Department of Mechanical Engineering, University of Bath, UK

Abstract

Unsteady aerodynamics of two flexible cantilevered wings in transverse gusts has been studied by means of force, velocity, and deformation measurements. The first bending frequencies of the wings were in the range of gust frequencies tested. The deformation measurements revealed that plunge angle due to the bending deflections is generally small. However, it becomes large at the resonant conditions and significantly attenuates the amplitude of the effective gust angle perceived by the wing, although the unsteady lift is difficult to measure accurately for the resonant cases. As the gust frequency increases, the more flexible wing experiences more separated flow during the cycle. Nevertheless, for both flexible wings, the lift amplitude normalized by the gust amplitude is smaller than those of the rigid wings with separated flows. When the maximum effective angle of attack is smaller than a critical value, the lift amplitude normalized by the gust amplitude is close to the theoretical predictions for attached flows and the effect of the gust reduced frequency is small. In contrast, above the critical value of the maximum effective angle of attack, the normalized lift can be amplified or attenuated, depending on the gust reduced frequency.

I. Introduction

The field of unsteady aerodynamics has been an important field of research for nearly a century. The effects of time-dependent relative vertical velocity variations caused by plunging (heaving) and pitching oscillations have been investigated to understand aeroelasticity of aircraft wings and rotorcraft blades, and to predict gust loads on fixed wings. Early unsteady aerodynamics models were developed in the 1930s based on the attached flow assumption (Theodorsen, 1935; von Karman and Sears, 1938; Sears, 1941). Later studies focused on flow separation, formation and shedding of leading-edge vortices, and the dynamic stall phenomenon (McCroskey, 1982; Ekaterinaris and Platzer, 1998), which is characterized by overshoot and hysteresis of lift and pitching moment when compared to static cases.

Estimation and alleviation of extreme forces and moments are essential to the design of lighter and more efficient aircraft. However, as aerostructures become lighter and more flexible, the extreme loads caused by atmospheric gusts and turbulence are gaining importance (Dowell, 2015) and the influence of flexible body response on the loads cannot be neglected. The consequences of the excitation of the structural modes by gusts have been recognized as early as 1970s when the jet flap was proposed as a fast-acting lift control device for gust alleviation (Simmons & Platzer, 1971). Recent investigations on loads control suggested alternative fast-acting devices based on mini-tabs and wall-jets (Al-Battal et al, 2019; Heathcote et al., 2020).

Most of the investigations of unsteady aerodynamics of transverse (heaving) and rotational (torsional) oscillations of wings are restricted to rigid two-dimensional airfoils mounted elastically (Dimitriadis and Li, 2009). However, a wing's finite span may cause several effects that are significant, including: three-dimensional time-averaged deformation (twisting and bending of wing sections), variations of the vibration amplitude and phase (and thus, effective angle of attack) in the spanwise direction, and three-dimensional unsteady flow over the wing. In an experimental study of a flexible high aspect ratio wing, it was found that the stall flutter and the limit-cycle oscillations were dominated by the unsteady aerodynamics of stall (Tang and Dowell, 2001). The fluid–structure interactions of a finite aspect ratio, cantilevered, flexible wing were investigated by Fagley et al. (2016) using a clever experimental set-up. They identified the stall flutter instability which was dominated by harmonic deformation in a single mode (torsion) and caused by coupling with the dynamic stall process. Culler et al. (2017) designed and tested a flexible wing model that exhibits torsion dominated limit-cycle oscillations, which were measured at four spanwise planes by using a stereo vision motion tracking system.

When a flexible wing encounters a gust, unsteady lift, drag and pitching moment cause deformation of the wing, which modifies the effective angle of attack as perceived by the wing as well as the vorticity shed into the wake. This problem is complicated by excitation of the bending and torsional modes, which introduce pitch and plunge oscillations that depend on the amplitude of the gust, the flexibility of the wing and the interaction of the gust frequency with the wing's natural frequencies. The excitation of a wing by a gust at or near its natural frequencies is of particular interest, as computational (Neumann & Mai, 2013) and experimental (Tang et al. 2010) studies unsurprisingly reveal strong amplification of the wing's deformation. Tang et al. (2010) tested an aeroelastic wing model, placed at small angles of

attack (0 to 2 deg at the root), with a flexibly suspended root support (to simulate rigid body modes) when the wing was subjected to a small-amplitude gust (less than 1.5 deg). The gust was created by placing a rotating slotted cylinder behind a fixed airfoil upstream of the wing model. In response to a harmonic gust, various structural frequencies can be excited, and the effect of the flexible mounting device at the wing root may be significant depending on the gust frequency.

Neumann and Mai (2013) investigated the aeroelastic response of a swept wing in the wake of an upstream pitching airfoil. This study was also restricted to small gust angles (less than 1 deg) and small deflections of the wing (maximum static deflections around 4% of the semi-span and unsteady deflections less than 2% of the semi-span). The transfer function of measured and simulated tip deflection as a function of gust frequency revealed the peak response (resonance) occurred near the first bending mode of the wing. Chen and Jaworski (2020) reported simulations of inviscid interaction of a point vortex with a downstream airfoil, which was elastically mounted and free to plunge in a single degree of freedom. It was shown that the trajectory of the vortex depends on its strength and initial upstream location, as well as the airfoil natural frequency. The transient interaction may induce an oscillatory damping of airfoil circulation and plunge displacement. Barnes and Visbal (2018) investigated the viscous interaction of a counterclockwise vortex with an elastically mounted NACA0012 airfoil at a Reynolds number of Re=150,000 and at an angle of attack of zero deg. The airfoil was mounted at the leading-edge and was free to oscillate in pitch. The transient interaction caused transition and a laminar separation bubble, and triggers laminar separation flutter.

All these previous computational and experimental investigations of gust-induced-excitation are generally limited to small deformations. At the other extreme lay the large deformations of flapping wings which oscillate near their natural frequencies. Chordwise and spanwise flexibility of the wings oscillated near the resonance conditions can enhance the lift and thrust (Shyy et al. 2010; Gursul et al. 2014) by modifying the leading-edge and trailing-edge vortices. When the root is sinusoidally plunged with small amplitude near the resonance frequency, the motion is amplified along the span, resulting in a larger tip motion but with a phase lag (Cleaver et al., 2016). One important consequence of such oscillations with relatively large deformation is large inertial forces, which are difficult to separate from the aerodynamic forces in experimental studies.

In this paper we focus on deformation induced by gusts. For large civil aircraft, the turbulence spectrum can reach peak-to-peak gust amplitudes of up to 3 deg at cruise conditions and 12 deg at the lower velocities of take-off and landing, with reduced frequencies at cruise of up to $k = 1$ (Heathcote, 2017), where $k = \pi f c / U_\infty$, f is the frequency, c chord length, U_∞ freestream velocity. On the opposite extreme are micro air vehicles, which tend to operate within the atmospheric boundary layer at much lower speeds and can therefore encounter much higher gust angles (Gursul, 2004). In this article we focus on small amplitude gust angles, using a novel gust generator that we recently developed (Fernandez et al. 2021).

The easiest approximate method of experimental simulation of gust encounters is the oscillation of the test model in a steady freestream. However, such methods are inadequate for use with flexible models, as the forced motion of the model will cause large inertial forces which are difficult to separate from the aerodynamic forces. Hence a gust generator becomes necessary to simulate gusts on a fixed model. A variety of methods are used in the literature such as oscillating upstream airfoils (Wilder & Telionis, 1998) and even wind tunnels with oscillating walls (Holmes, 1973). The high inertia of oscillating gust generators can make these unsuitable for the high-frequency gusts in wind tunnels. In addition, two-dimensionality of the gusts cannot be guaranteed if the gusts are produced by shear layers, i.e. jets, wakes, and shed vortices. Instead, an irrotational gust generator that rely on the deflection of freestream is likely to produce more two-dimensional gusts.

The present study was conducted using a novel "irrotational" gust generator (Fernandez et al. 2021), called the 'oscillating fence' rig, that can produce repeatable, periodic gusts using a small lightweight fence which can be oscillated at high frequency. The lift, flow field and deformation of two flexible wings were measured for steady ($k = 0$) and unsteady ($k = 0.017 – 0.181$) small-amplitude gusts at geometric angles of attack at the root $\alpha_0 = 0^o$, 5^o, 10^o, 12^o. The wings have different rigidities which were prescribed such that their natural first bending frequencies lie within the range of gusts tested. The effect of wing deformation on the effective gust angle felt by the wing as well as lift change normalized by gust amplitude were investigated. Lift of the flexible wings was also compared with similar data from an equivalent rigid wing.

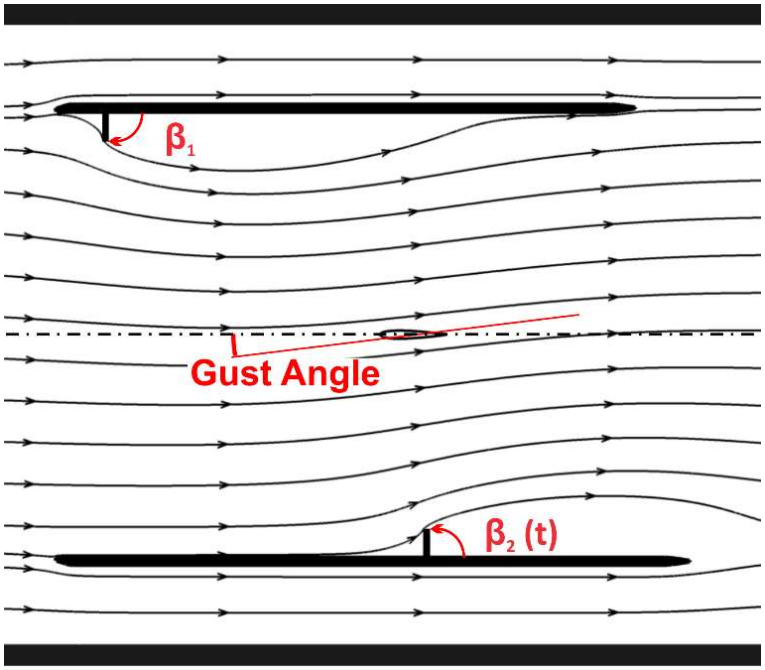

Figure 1: Gust generator concept showing upstream and downstream fence deployment angles, β_1 and β_2 respectively.

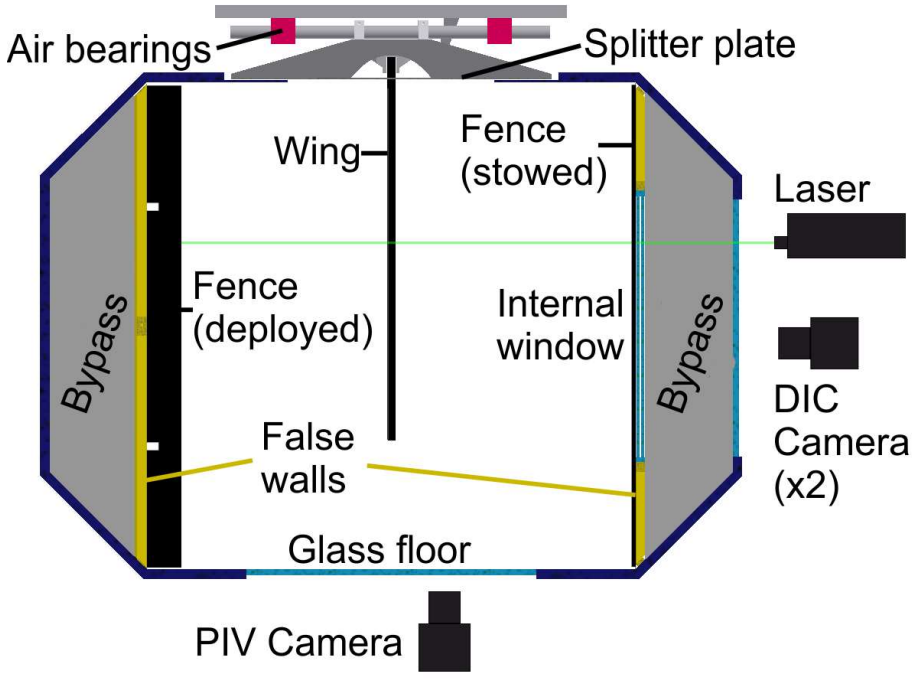

Figure 2: Model of the wind tunnel cross section showing the wing and mount structure, the false walls with the upstream and downstream fences stowed and deployed respectively, and the camera and laser set up for the PIV and DIC systems.

II. Methods

The present study was performed in the high-speed section of the large closed loop wind tunnel at the University of Bath, which is capable of up to 30 m/s freestream velocity in its 2.13 x 1.52 m^2 octagonal cross section. A pitot probe at the working section entrance measured freestream velocity. The freestream velocity was U_∞ = 20 m/s and the Reynolds number based on the chord length was Re = 315,000.

A. Gust Generating Rig

The present experiments were carried out using a novel gust generator which produces periodic, small-amplitude flow deflections (Fernandez et al. 2021). The fundamental concept, presented in Figure 1, is to use two aerodynamic fences which are deployed from staggered locations on the wind tunnel walls, resulting in deflected freestream as the fence angle β increases from 0° to 90°. The small, lightweight fences can be simultaneously driven at high frequency to produce time-variant β_1 and β_2 histories. However, in the present study β_1 was kept constant at either 0° or 90°, while β_2 was driven periodically in sinusoidal motion.

Figure 2 shows a schematic of the experimental set up. Two false walls were introduced which allow a portion of the freestream flow to bypass the gust generator, converting the octagonal working section into a 1.52x1.52 m^2 square. The false walls are 32 mm thick welded aluminium frames with riveted aluminium skins and are comprised of five sub-structures which are assembled in-situ and house the aerodynamic fences when stowed ($\beta_1 = \beta_2 = 0°$). Each aerodynamic fence is a sandwich panel, with 2 mm carbon fibre skins and a 5 mm thick closed-cell foam core, which spans the width of the false walls and deploys to a height of 107 mm from the wall surfaces.

Each fence has a dedicated crank mechanism, which uses a 6 kW servo motor (ABB BSM100C) to power a pulley and flywheel through a low-backlash timing belt. The pulley and flywheel each have a push rod which drives a carriage on linear bearings, converting the rotation of the cranks into reciprocating motion which is then transmitted to the fence by a second set of push rods. A window in one of the false walls grants optical access to the test section. A detailed description of the gust generator and drive mechanism is given in (Fernandez et al. 2021), which also presents the calibration and measurement of the gust angle

α_g. The gust amplitude varies in the range of 3.9° to 6.2°, depending on the gust generator configuration and frequency. The gust shapes are presented later in the article.

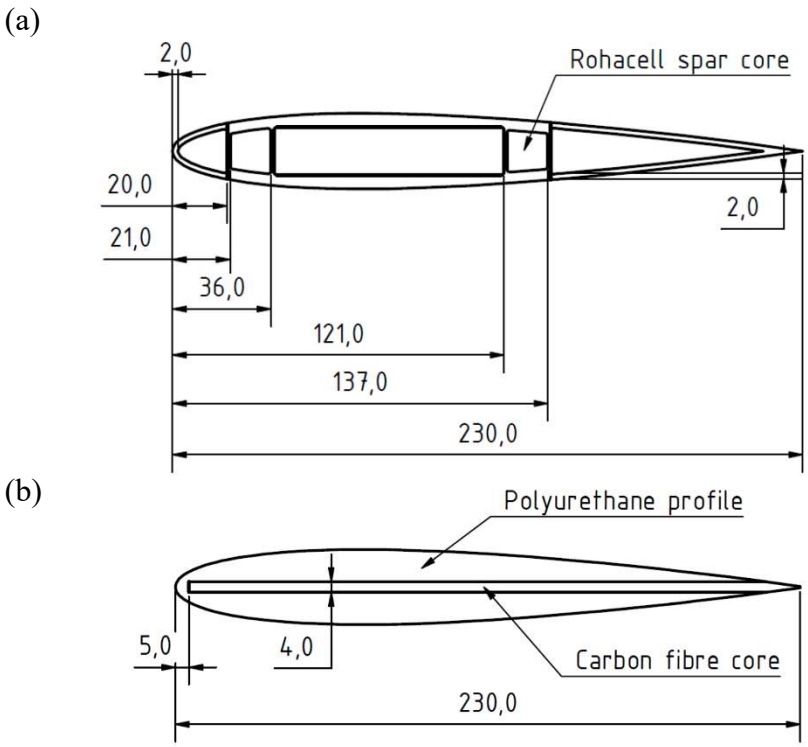

Figure 3: Cross section of the internal structure of the rigid (a) and high-flexibility (b) wings. Dimensions are in mm.

B. Wing Models

Three wing models were tested, one rigid and two flexible, all of which were rectangular wings with chord c = 0.23 m, semi aspect-ratio sAR = 5 and a NACA0012 cross section. This study focuses on the aeroelastic response of the flexible wings, but rigid wing results (reported by Fernandez et al. 2021) are included for comparison only. The wings were supported vertically in the test section on air bearings oriented in the cross-stream direction to allow the free transmission of lift into a one-component load cell. The wing mount features a splitter plate which isolates the ceiling immediately surrounding the wing from the wind tunnel structure. The rigid wing was a carbon fibre semi-monocoque with 2 mm skins and two internal spars which formed an extremely rigid box section, as shown in Figure 3 (a). The flexible wings were manufactured from polyurethane rubber moulded over a carbon-fibre flat plate as shown in Figure 3 (b) for the high-flexibility wing. The carbon plates, which provide almost all the

rigidity, run the length of the chord with a small, 5 mm clearance from the leading edge to prevent the polyurethane from peeling away at this location. The densities of the wings are 1080 kg/m^3 (low flexibility) and 1070 kg/m^3 (high flexibility).

Our structural model assumed the carbon spar of the wings was the only rigid component of the structure. The flexural stiffness was calculated as $3EI/L^3$, while the torsional stiffness was GJ/L (Thorby 2008). Here E denotes Young's modulus (210 GPa), I is the moment of inertia of the carbon spar, L is the length of the beam, G is the shear modulus (5 GPa) and J is the polar moment of inertia of the beam. Thus, the low-flexibility wing had a flexural rigidity of 1190 N/m and a torsional stiffness of 2.34×10^4 Nm/rad, while the high-flexibility wing had a flexural rigidity of 679 N/m and a torsional rigidity of 1.94×10^4 Nm/rad. The wing stiffnesses were chosen to obtain natural bending (1st mode) frequencies near 3.5 Hz and 2 Hz for the low and high flexibility wings respectively. These were chosen to coincide with the mid-range gust frequencies tested. The plates were laid up in 0-90 orientation and had thicknesses of 6.4 mm and 4 mm after curation. For the low and high-flexibility wings, the measured natural bending frequencies after curing were 3.42 Hz and 1.90 Hz respectively.

C. Force, Velocity and Deformation Measurements

Lift measurements were taken by a one-component miniature load cell (Futek LSB200Jr - FSH00105) with a 25 lb measurement range. Steady measurements were 20,000 samples at 1 kHz, while unsteady measurements were 50 cycles at 1,000 samples/cycle. The force signal was recorded alongside the encoder signal from the gust rig's servo drive to determine the phase of measured lift. This was acquired by a National Instruments cRIO-9076 running a Labview program on the RealTime and FPGA environments for high-speed acquisition.

Particle Image Velocimetry (PIV) measurements captured the time-averaged flow field under steady gust conditions (k=0) and the phase-averaged flow in unsteady gusts (k=0.017 – 0.181). The flow was seeded with olive oil droplets from a TSI oil-droplet generator. A TSI 2D-PIV system was used with a Quantel Evergreen 200 mJ 15 Hz Nd:YAG laser, a single CCD camera (TSI PowerView 8MP) and a TSI LaserPulse synchronizer. The laser was fitted with a cylindrical lens and aligned with the mid-span plane, while the laser sheet was recorded by the camera from underneath the glass floor, as shown in Figure 2. Unsteady measurements were individually triggered by the cRIO, which monitored the gust rig's servo position to output trigger pulses at the desired phase. Averages of 100 images were taken. A program was written

in Matlab using the 'fminsearch' function to match the theoretical NACA 0012 profile to the intersection of the laser sheet with the wing, giving the instantaneous positions of the wing section which are presented in the phase-averaged views.

A stereoscopic Digital Image Correlation (DIC) system was used to record the 3D deformation of the flexible wings under steady and unsteady gust conditions. In this method, a random speckle pattern is sprayed onto the model surface, as shown in Figure 4 (a), and recorded by multiple cameras which are calibrated such that their position relative to the test section is known. By matching the speckle patterns of the different images, the painted surface can be reconstructed in 3D as shown in Figure 4 (b). A LaVision low-speed DIC system was used with two CCD cameras (Imager M-Lite 4MP), a programmable Timing Unit (PTU-X) and a PC running DaVis 8. Acquisition was performed at 50 Hz for 20 s with an uncertainty in cross-stream deflection no more than 0.1%c. The cameras were triggered continuously by the PTU's internal timer after receiving the 'start' command, which was sent by the cRIO when the rig was in its stowed position (t/T=0, β_2=0°). The raw surface data was then converted into deflection and twist of the mid-chord by matching a NACA0012 profile to each spanwise segment of the extracted surface. Due to a lack of optical access to the wing root, the inboard 350 mm of the span were not captured by the DIC system and had to be extrapolated. This was done by fitting a quadratic curve to the mid-chord line with zero gradient at the root. Twist was assumed to vary linearly in this region. Deflection and twist (with respect to the undeformed wing cross-section at a fixed angle attack α_0 at the root) were then integrated over the span to yield spanwise-averaged deflection and twist, which are the basis for all deformation data given in this article. The spanwise-averaged twist angle α_t and cross-stream velocity h both modify the effective angle of attack at the gust angle α_g:

$$\alpha_{eff} = \alpha_0 + \alpha_g + \alpha_t + tan^{-1}\left(-\frac{1}{U_\infty}\frac{dh}{dt}\right)$$

The inertial force F_{INERT} acting on the load cell is calculated as the product of the spanwise-averaged cross-stream acceleration and the mass of the wing:

$$F_{INERT} = m\,\frac{d^2h}{dt^2}$$

Hence the aerodynamic lift coefficient is calculated from the measured total force as follows:

$$C_L = \frac{(F_{MEASURED} - F_{INERT})}{0.5\,\rho {U_\infty}^2 S}$$

where ρ is the density and S is the planform area.

Due to the relatively low sampling rate of the DIC measurements (50 Hz) compared to the lift measurements (0.5 – 5 kHz) it was necessary to approximate the spanwise-averaged deformation of the wing using a 4^{th}-order Fourier series which was used to estimate the deflection and twist at any given phase. The cross-stream velocity and acceleration of the wing were calculated as numerical derivatives of the deflection. However, in order to minimize the numerical errors, the cross-stream velocity and acceleration were calculated using the first two terms of the Fourier series only. The Fourier coefficients had error bounds of no more than 0.6% for a 95% confidence level.

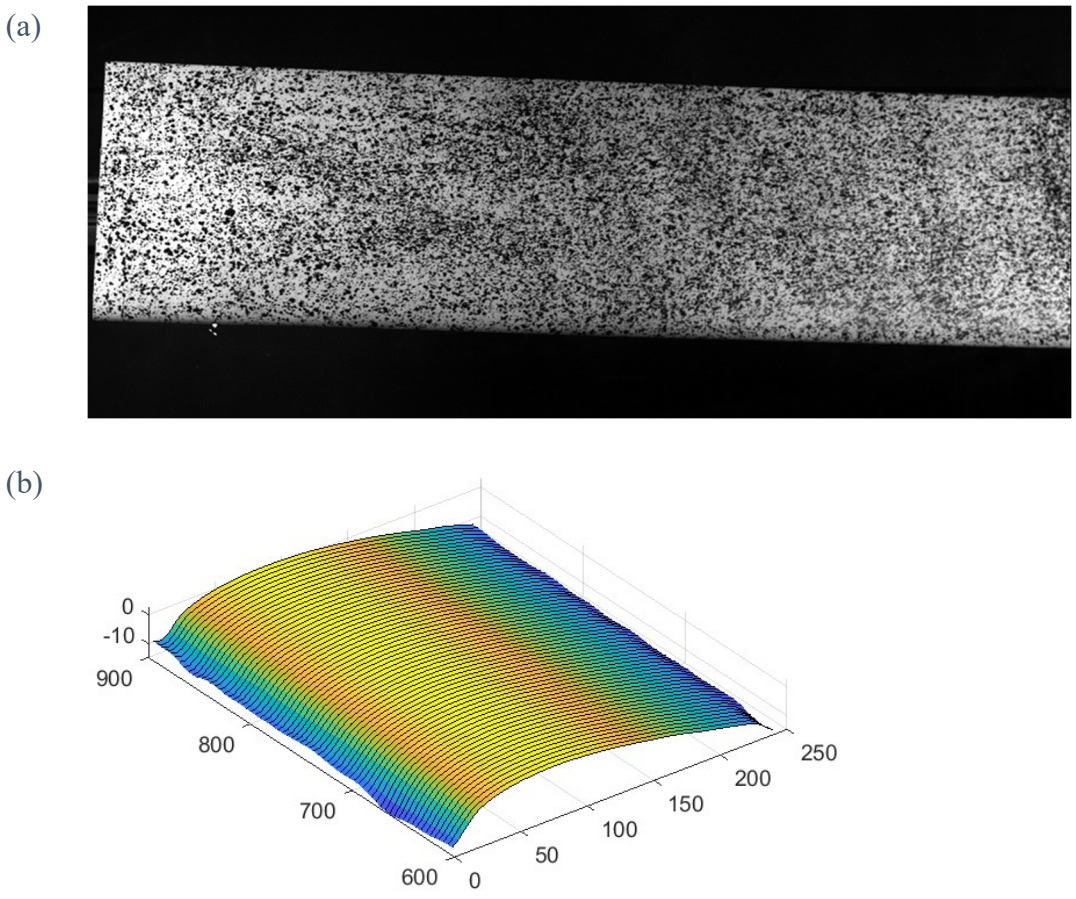

Figure 4: (a) DIC image of the high-flexibility wing under aerodynamic load and (b) a sample of the extracted surface. Dimensions are in mm.

III. Results

A. Wings in Steady Gusts ($k = 0°$)

In this section, we present the lift coefficients, flow fields, and wing deformation in "steady gusts", which correspond to steady flow deflections produced by the gust generator when its aerodynamic fences are deployed to steady β_1 and β_2 values. Figure 5 compares the mean lift coefficients for steady gusts ($k = 0$) at geometric angles of attack $\alpha_0 = 0°, 5°, 10°, 12°$ with β_1 held at either 0° or 90°, denoted here by closed and open markers respectively, and varying β_2 from 0° or 90°. These data are accompanied by the mean lift coefficients of the same wings in an undisturbed freestream ($\alpha_g = 0^o$) and varying geometric angle of attack α_0, and is denoted by the solid black line. A wide range of α_0 was covered to include pre- and post-stall angles of attack. The data are presented separately for each wing. Figure 5a shows these data are shown for the rigid wing. The steady gust data agree well with the baseline lift curve below stall, but as α_{eff} approaches the static stall angle of 12.5° the steady gust case appears to stall slightly later and at a higher C_L. This was attributed to alleviation of the suction-side pressure gradient due to mild spatial non-uniformity of the gust. Similar data are shown in Figure 5b for the low flexibility wing. Here, the baseline lift is seen to rise to a higher value near $\alpha_{eff} = 14^o$, which is followed by a momentary drop in lift but develops a second rise in lift until its maximum value at $\alpha_{eff} = 18^o$. The steady gust data follow the same approximate trend but develop a slightly lower lift slope than the baseline curve for $\alpha_{eff} > 5^o$ which ends in a flattened lift peak, instead of the pronounced double peak of the baseline curve. Compared to the rigid wing, lift variations in the post-stall region are more gradual. Conversely, the lift of the high flexibility wing, shown in Figure 5c, stalls at a much lower incidence near $\alpha_{eff} = 11^o$. The steady gust and baseline lift rise along the same gradient but disagree in the post-stall region. For all three wings the lift at $\alpha_{eff} = 0^o$ is very slightly negative, most likely due to slight flow asymmetry within the gust generator.

Figure 6a shows an expanded view of the lift near the stall for the low flexibility wing. Sample flow fields from time-averaged PIV measurements are shown in Figure 6b for two cases. At $\beta_1=0^o$, $\alpha_0=12^o$ the flow separates from the leading-edge between $\alpha_{eff} = 14.2^o$ and 15.3^o, forming a large bubble of recirculation which is accompanied by a mild drop in C_L. Similarly, for $\beta_1=90^o$, $\alpha_0=10^o$ flow separation occurs between $\alpha_{eff} = 15.1^o$ and 16.9^o where a decline in C_L is seen. The lift of the high flexibility wing, given in Figure 6c, has more pronounced stall which

occurs near $\alpha_{eff} = 12^o$ for steady gust cases. The time-averaged PIV images in Figure 6d are in rough agreement, showing flow separation between $\alpha_{eff} = 12.1^o$ and 12.5^o for $\beta_1=0^o$, $\alpha_0=12^o$; and between $\alpha_{eff} = 12.5^o$ and 13.5^o for $\beta_1=90^o$, $\alpha_0=10^o$. In both cases, the time-averaged flow separation region appears smaller compared to the low flexibility wing. Due to the large bending deflections experienced by the high flexibility wing, the under-floor camera location

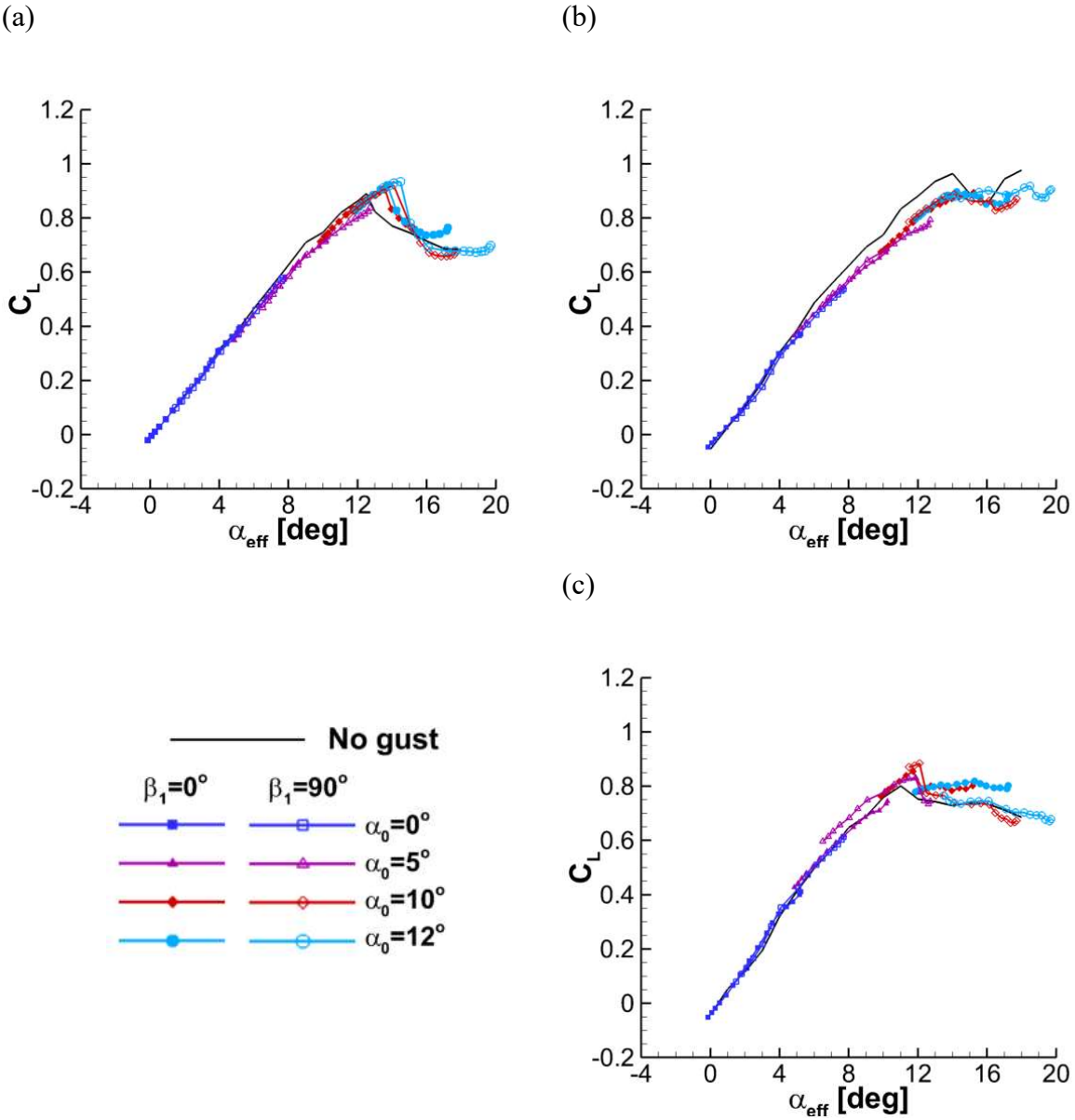

Figure 5: Steady lift coefficient for the (a) rigid, (b) low-flexibility and (c) high-flexibility wings at $\beta_1=0^o$, 90^o.

was unable to view the wing's suction surface in a number of cases. For these cases the camera had to be relocated to above the wing root. This area was not originally intended for such a

purpose and had limited mounting options, leading to a reduced field of view as seen in the PIV images. Another consequence of the high flexibility of the wing is the scatter seen in the instantaneous wing surface profiles, resulting in the appearance of thicker lines, and is due to the excitation of the wing's flexible modes by the separated flow. The wing vibrations in this case might also have contributed to the increased mixing and smaller separated flow regions in the time-averaged flow.

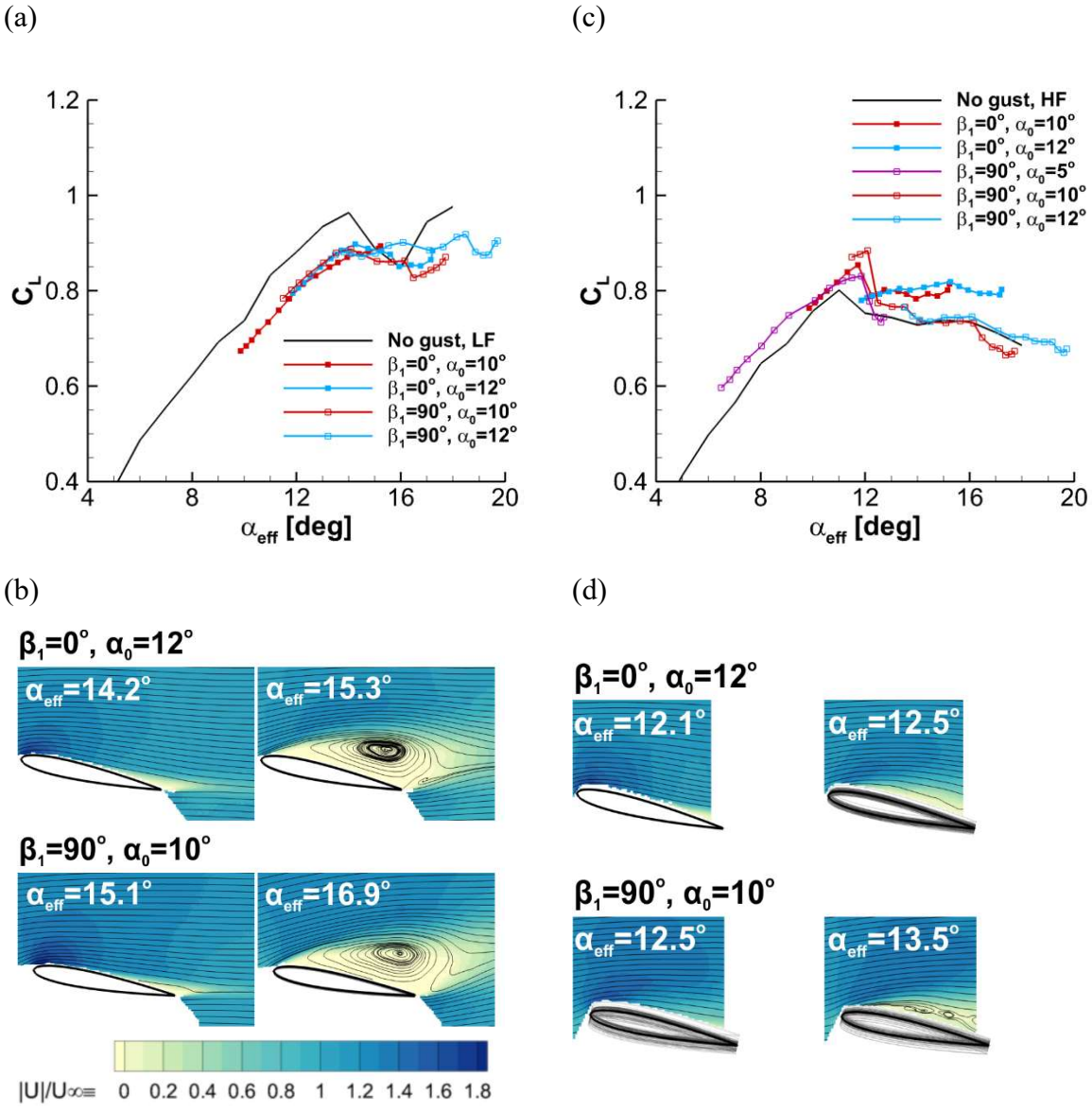

Figure 6: (a) Steady lift of the low-flexibility wing and (b) time-averaged PIV near stall; (c) steady lift of the high-flexibility wing and (d) time-averaged PIV near stall.

Figure 7a shows the spanwise-averaged cross-stream deflection h of the low flexibility wing as a function of ($\alpha_0 + \alpha_g$) for steady gusts, and is nondimensionalized by wingspan b. Error bars

of standard deviation are included, though in this case the deviations are too small to see. The deflection increases proportionally with ($\alpha_0 + \alpha_g$) at first, but plateaus near ($\alpha_0 + \alpha_g$) = 15°. The spanwise-averaged twist angle α_t is shown for the same wing in Figure 7b. The wing twist rises with aerodynamic load until ($\alpha_0 + \alpha_g$) = 13° above which it declines, while the error bars in this region suggest torsional oscillations which rise with ($\alpha_0 + \alpha_g$) to values of the order of ±2°. It is possible that these oscillations are responsible for the sustained lift seen at high α_{eff} for the

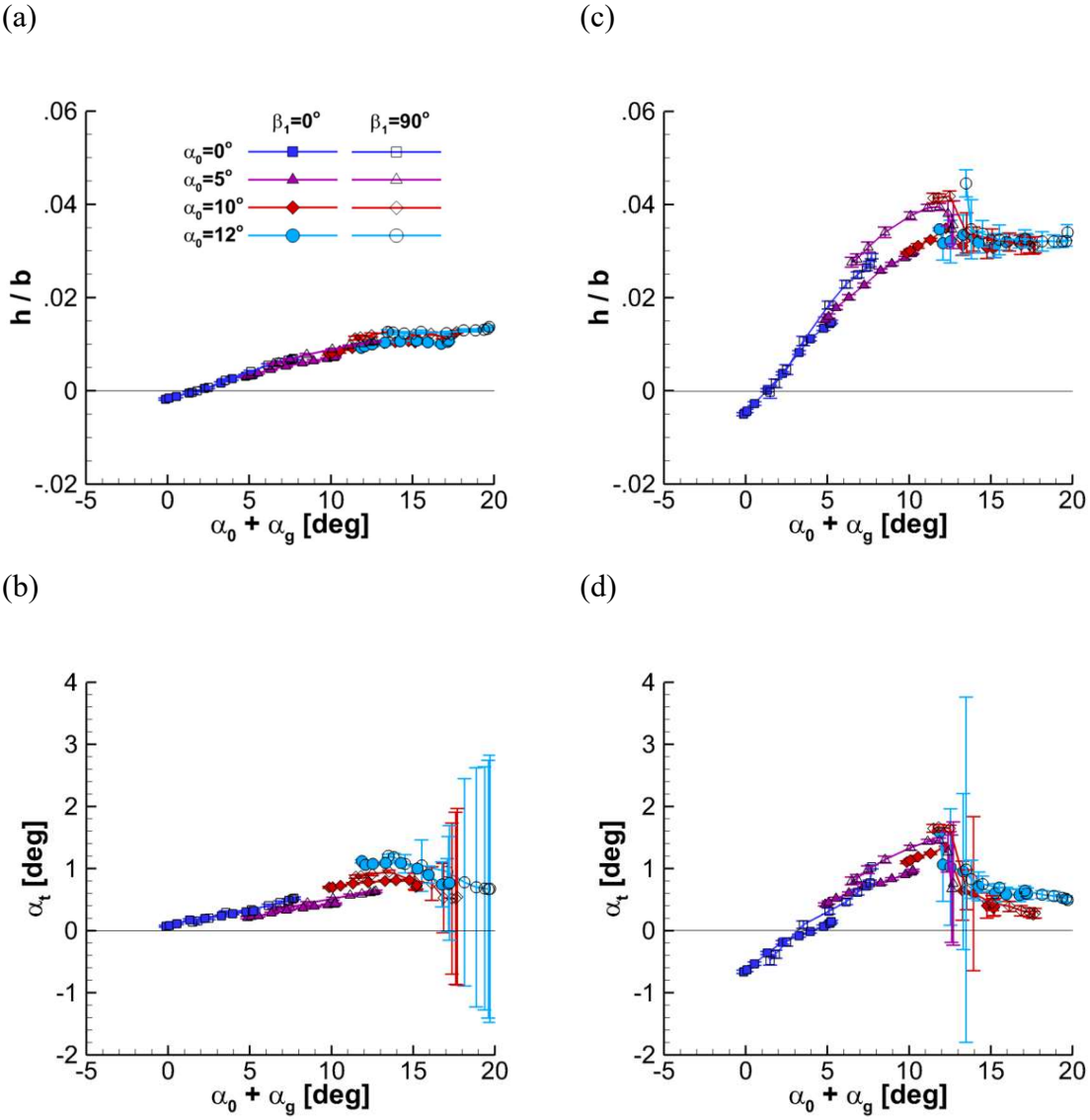

Figure 7: (a) Spanwise averaged cross-stream deflection and (b) spanwise averaged twist angle for the low-flexibility wing; (c) spanwise averaged cross-stream deflection and (d) twist angle for the high-flexibility wing. Error bars denote standard deviation of the variable.

low flexibility wing. Similar observations of self-excited wing oscillations increasing the lift is well known for the separated flows over flexible delta wings (Taylor et al. 2007). For the high flexibility wing the cross-stream deflection, shown in Figure 7c, is significantly more sensitive to aerodynamic loads and clearly shows a trend similar in shape to the static lift coefficient of Figure 6c. Error bars show a rise in bending oscillations for $(\alpha_0 + \alpha_g) = 12^o$ to 15^o, immediately following the sudden drop of *h/b,* which is consistent with the stall of C_L. The high flexibility wing's twist angle, shown in Figure 7d, follows the same trend and exhibits large-amplitude torsional oscillations which, unlike the low flexibility wing, peak immediately after the stall of *h/b*, and have mostly died out by $(\alpha_0 + \alpha_g) = 15^o$.

B. Wing Deformation in Unsteady Gusts

This section will present the spanwise-averaged deformation of the flexible wings in gusts of varying frequency in the range $k = 0.018$ - 0.181 at $\alpha_0 = 0^o$, 5^o, 10^o, 12^o. The variations of the spanwise-averaged twist angle, cross-stream velocity due to the bending oscillations, and the effective angle of attack are presented in a gust period, while the gust shape and wing angle of attack are varied. The gust amplitude and phase are highly dependent on frequency, as shown in Figure 8a for $\beta_1 = 0°$. Here the phase angle is related to the fence angle β_2 (Fernandez *et al.* 2021), which allows us to compare the unsteady gust data to the steady gust data at equivalent phases.

Figure 8a shows the unsteady gust angle α_g as a function of phase for varying k at $\alpha_0 = 0°$ and $\beta_1=0^o$. Here the phase angle is related to the fence angle β_2 (Fernandez et al. 2021). The cross-stream deflection of the low flexibility wing in response to these gusts is shown in Figure 8b for $\alpha_0=0^o$, $\beta_1=0^o$. Except for $k = 0.126$, the bending deflections are very small. At this reduced frequency, the resonance with the wing's natural bending frequency of $k_n = 0.123$ leads to *h/b* exceeding all other cases by a substantial margin. Figure 8c shows similar data for the high flexibility wing at $\alpha_0=0^o$. The deflections here are expectedly larger but behave in a similar way. At $k = 0.072$ resonance with the natural bending frequency of $k_n = 0.062$ produces an amplified lift response with a large lag.

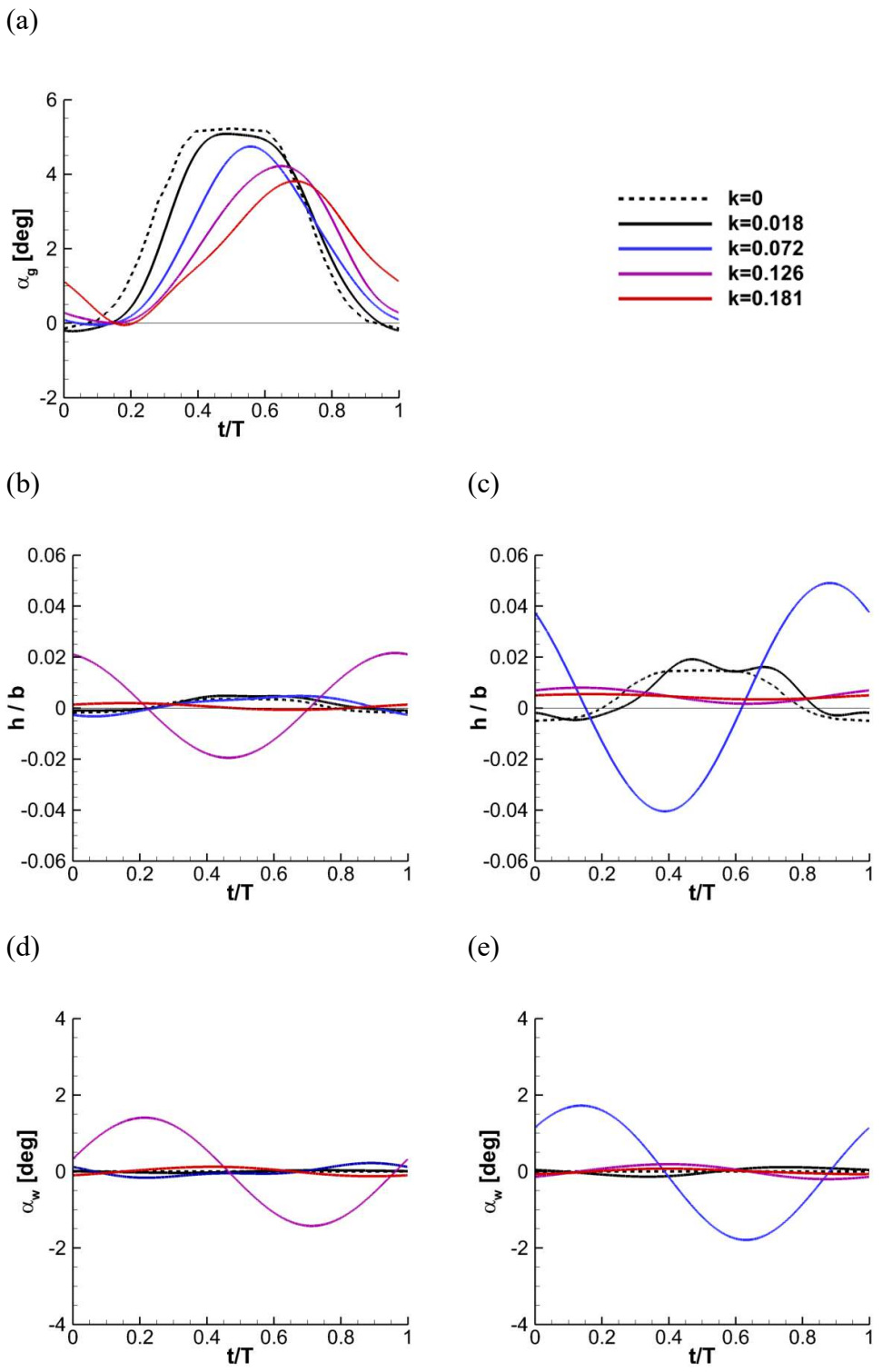

Figure 8: Response for varying k at α_0=0°, β_1=0°. (a) Gust profile. (b) Cross-stream deflection of the low flexibility and (c) high flexibility wings. (d) Plunge angle of the low flexibility and (e) high flexibility wings. (f) Twist angle of the low flexibility and (g) high flexibility wings (h) effective angle of attack for the low-flexibility and (i) high flexibility wings.

(f) (g)

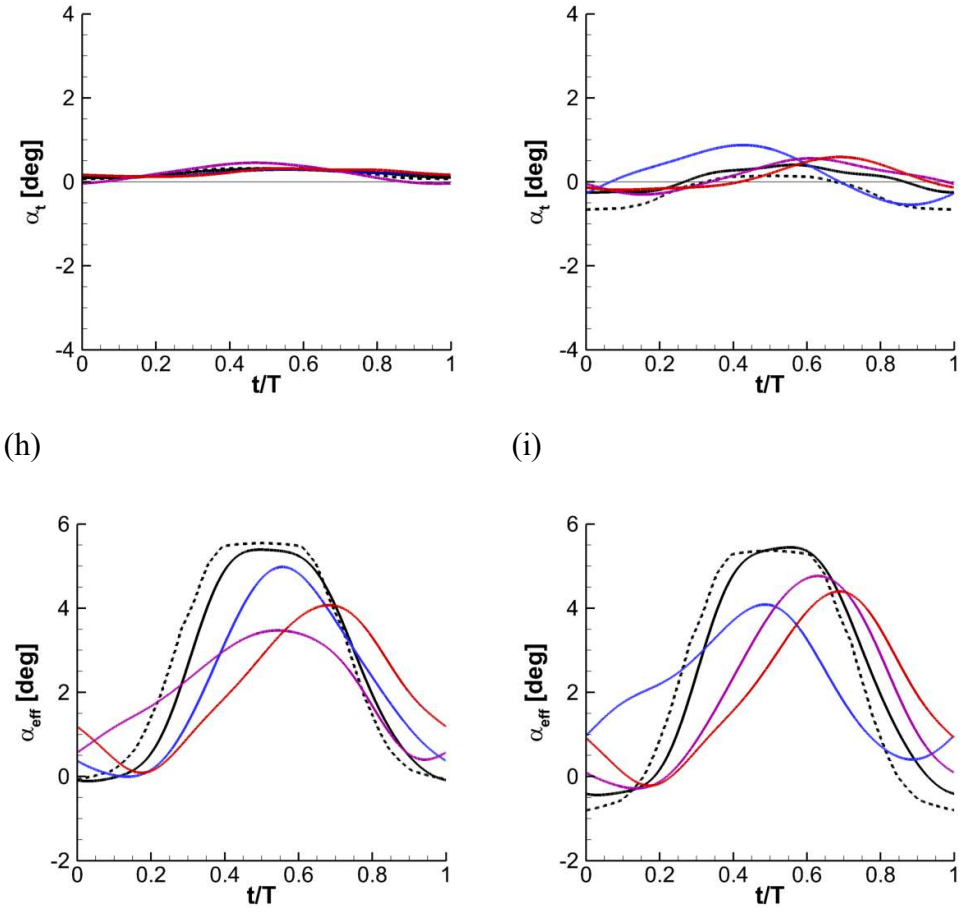

Figure 8 continued.

The plunge angle α_w due to the bending oscillations,

$$\alpha_w = tan^{-1}\left(-\frac{1}{U_\infty}\frac{dh}{dt}\right)$$

for the aforementioned cases is shown for the low flexibility wing in Figure 8d. It is generally small, except at $k = 0.126$, which is near the resonance frequency. For the high flexibility wing, the behaviour is similar, as shown in Figure 8e. The non-resonant cases produce small values of less than ±0.5°, but large oscillations of roughly ±2° occur at $k = 0.072$ due to the wing's amplified plunging motion.

Figure 8f shows the twist angle α_t of the low-flexibility wing for varying k. Overall values are small, even at resonance, and do not have a significant effect. The high flexibility wing is more susceptible to twisting, as shown in Figure 8g, with peak-to-peak amplitudes of near 1° for non-resonant cases and 2° for the resonant $k = 0.072$. The variation of the effective angle of attack for α_0=0° and varying k is shown in Figure 8h for the low flexibility wing. Comparison with

the gust angle α_g profiles of Figure 8a gives a clear indication of the effects of aeroelasticity on the perceived gust profile. The two trends are reasonably similar for k = 0.018, 0.072 and 0.181, but at k = 0.126 the plunge angle relieves the effective angle of attack α_{eff}, resulting in a more gradual rise and smaller amplitude when compared to α_g. The same behaviour was observed on the high flexibility wing, as shown in Figure 8i, where the k = 0.072 case exhibits a particularly shallow rise in α_{eff} with a significantly lower amplitude when compared to α_g.

The unsteady gust angle for β_1=90° is shown in Figure 9a for varying k. The profile shapes are like those for β_1=0°, albeit with slightly higher overall values, so the results described here share many features with the lower incidence results described previously. The cross stream deflection of the low flexibility wing is shown in Figure 9b for α_0=12°, β_1=90°. Apart from a slightly higher mean value due to the increases in α_0 and α_g, the h/b curves are similar to those of the same wing at α_0=0°, β_1=0°. Figure 9c shows similar data for the high flexibility wing, which is more sensitive and reaches a higher mean deflection at all frequencies. For both wings, the amplitude of bending oscillations is small, except near the resonance frequencies. In particular, at k = 0.067, resonance with the wing's natural bending frequency becomes dominant and produces large plunging oscillations.

The plunge angle α_w is shown in Figure 9d and Figure 9e for the low and high flexibility wings respectively. These are virtually unchanged from to the lower incidence cases, shown in Figure 8d and Figure 8e, as this parameter is primarily dependent on k. Twist angle α_t, shown in Figure 9f and Figure 9g for the low and high flexibility wings respectively, has increased to approximately 1° in both cases, but the variations of the curves are similar to those for α_0=0°, β_1=0°. The effective angle of attack, shown in Figure 9h and Figure 9i for the low and high flexibility wings respectively, has risen substantially but still follows the same shape as α_g, with the exception of resonance cases which exhibit reduced amplitude and slope due to the large α_w components. Thus, while geometric angle of attack has some effect on the aeroelastic behaviour of the wing, the interaction of the gust frequency with the wing's natural frequency appears to play a dominant role at all incidences.

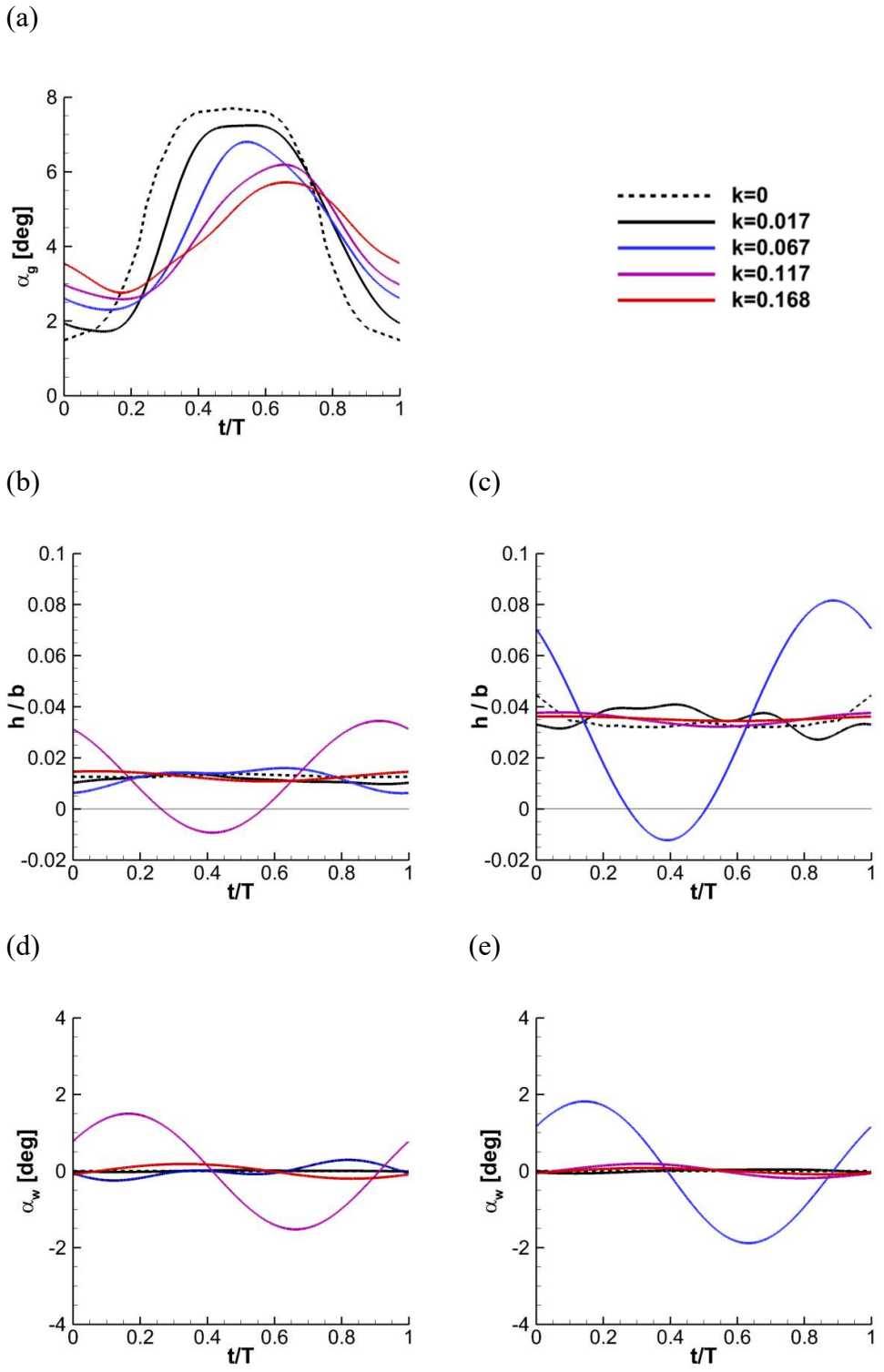

Figure 9: Response for varying *k* at α_0=12º, β_1=90º. (a) Gust profile. (b) Cross-stream deflection of the low flexibility and (c) high flexibility wings. (d) Plunge angle of the low flexibility and (e) high flexibility wings. (f) Twist angle of the low flexibility and (g) high flexibility wings (h) effective angle of attack for the low-flexibility and (i) high flexibility wings.

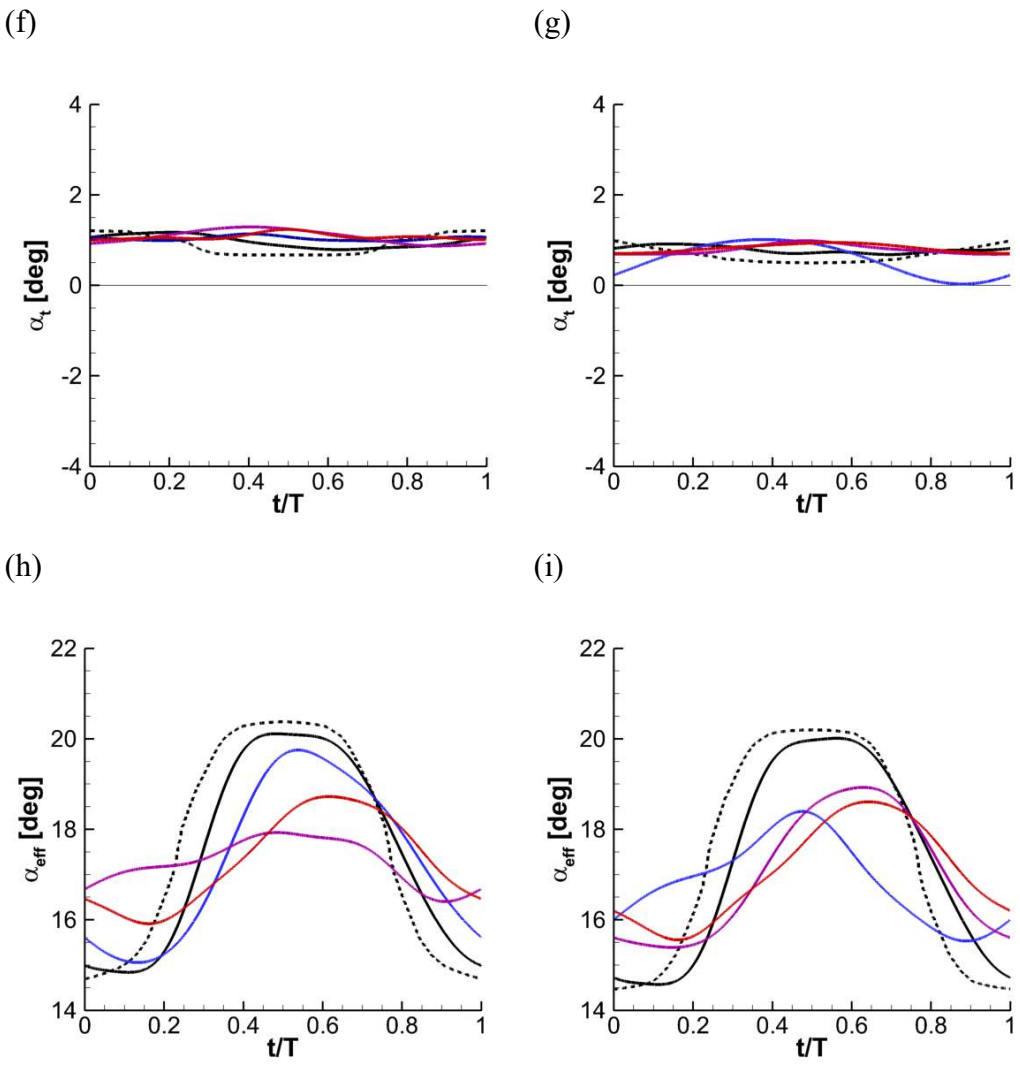

Figure 9 continued.

C. Gust Effectiveness

The gust effectiveness, defined as the ratio of the amplitude of α_{eff} to the amplitude of the gust α_g, grants further insight into the effects of flexibility on the perceived gust amplitude. Figure 10a shows this parameter for the low-flexibility wing. It is noted that "gust effectiveness" is derived based on the deformation measurements only, although aerodynamic forces obviously contribute to it. It is evident that, when k is not near k_n, gust effectiveness is near unity and there is little effect due to flexibility, but as $k \rightarrow k_n$ the alleviation of gust angle by large-amplitude plunging motion results in a large reduction in the effective gust amplitude. The high flexibility wing exhibits similar behaviour, as shown in Figure 10b. There is a slight trend towards higher effectiveness at lower α_0.

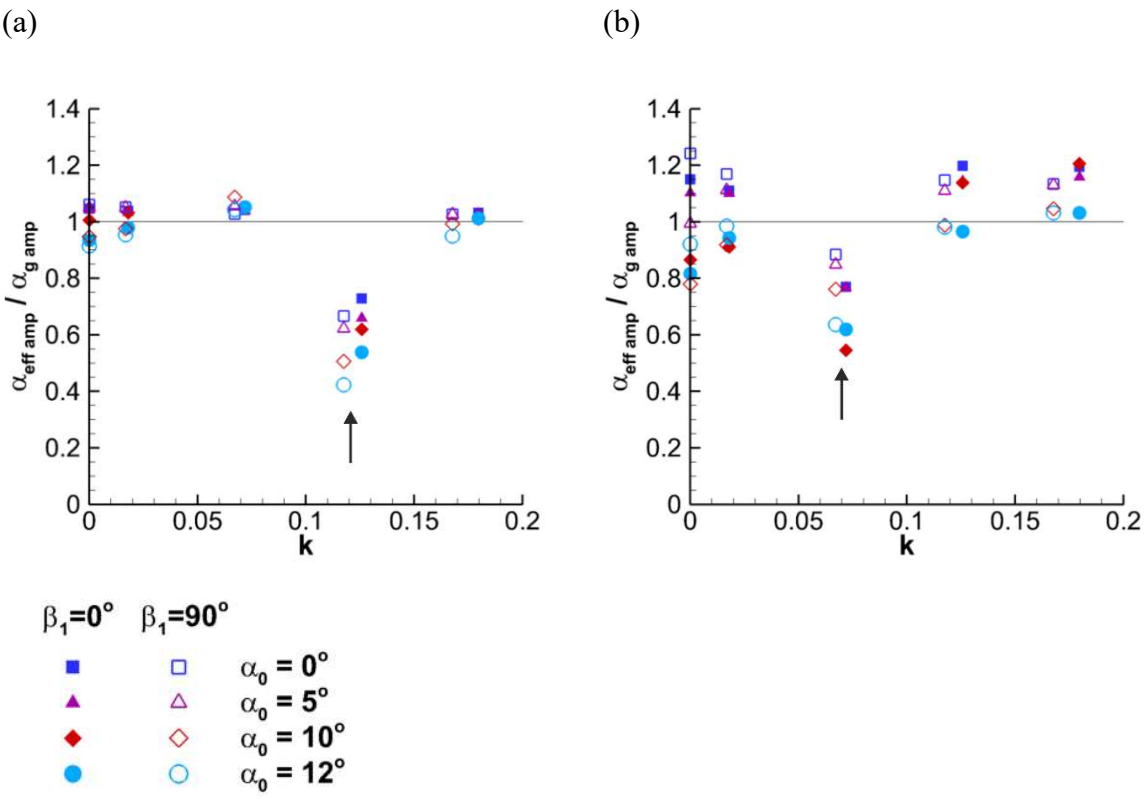

Figure 10: Gust effectiveness of the (a) low-flexibility and (b) high-flexibility wings. Arrows indicate the resonant cases.

D. Unsteady Lift and Flow Fields

As the gust angle time history is strongly dependent on the reduced frequency, we begin the analysis with the smallest reduced frequency k = 0.018. Figure 11a shows ($\alpha_{eff} - \alpha_0$) and lift coefficient as a function of t/T as well as the loops of C_L as a function of α_{eff} for varying α_0 at β_1=0° and k = 0.018. Here it is evident that ($\alpha_{eff} - \alpha_0$) is insensitive to geometric angle of attack, with all cases following the same approximate shape with a slight shift at higher α_0 as the wing deforms. The inertial force component caused by the cross-stream acceleration of the wing, is negligible when compared to aerodynamic lift coefficient C_L. Aerodynamic lift coefficient C_L plotted against α_{eff} produces loops which are aligned with the steady lift slope at low α_{eff}. However, at α_0=10°, C_L shows slight clockwise hysteresis due to the onset of stall, and at α_0=12° it forms a distinct, clockwise loop centred around the post-stall region of the steady lift curves with a pronounced overshoot of the lift, ending in the sudden drop of C_L. Figure 11b shows similar information for the high flexibility wing. Here, the ($\alpha_{eff} - \alpha_0$) curves are less orderly than seen on the low flexibility wing, due to its greater sensitivity to the torsional moment, but

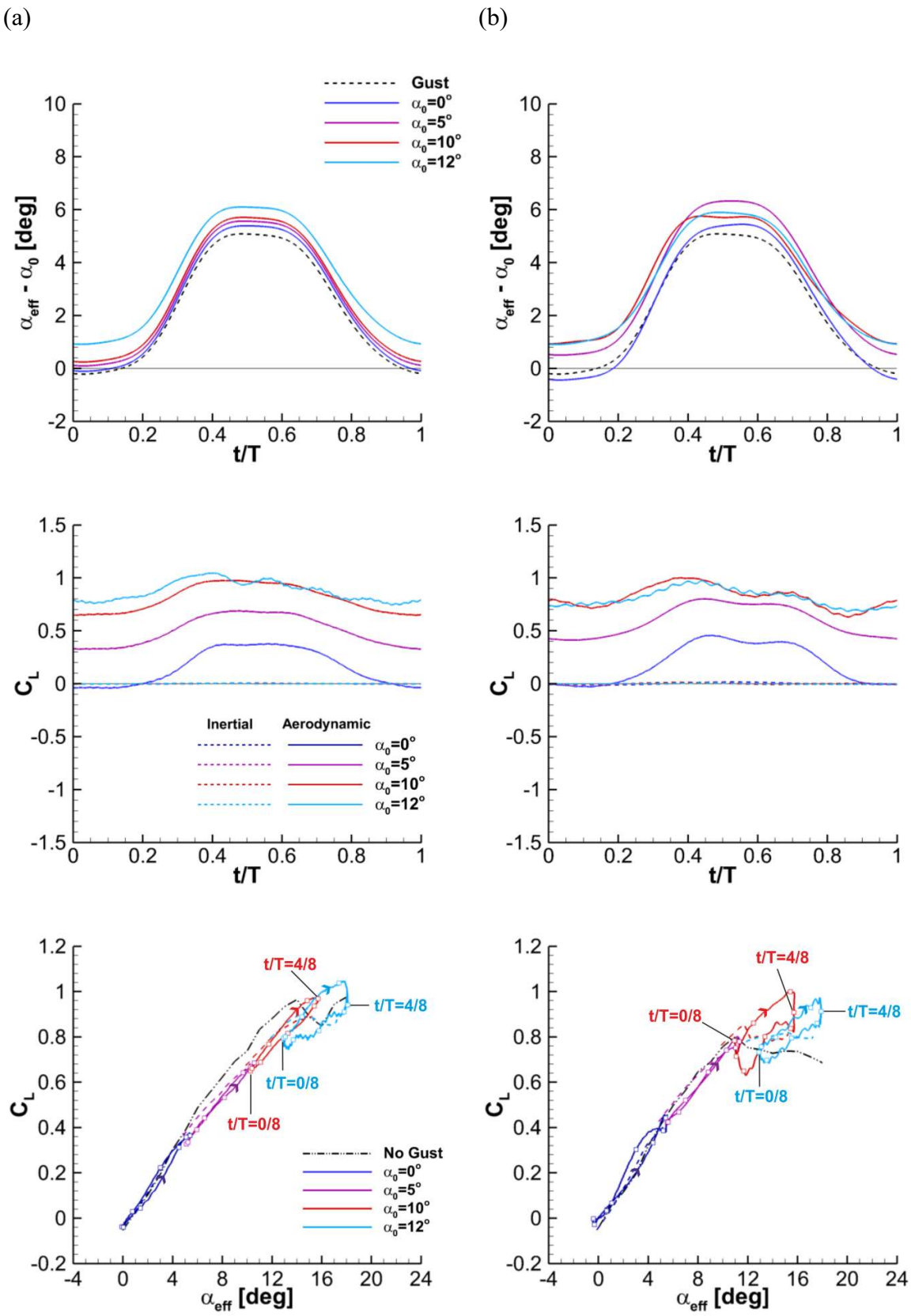

Figure 11: Comparison of effective gust angle, inertia force and aerodynamic lift for the (a) low-flexibility and (b) high-flexibility wings at β_1=0°, k=0.018.

follow the same trend. Likewise, the inertial loads are negligible, while aerodynamic C_L forms clockwise loops at $\alpha_0 \geq 10^o$. However, due to the lower stall angle of this wing, we see lift overshoot, clockwise hysteresis and pronounced stall at $\alpha_0=10^o$ which was not seen until $\alpha_0=12^o$ on the low-flexibility wing.

(a) (b)

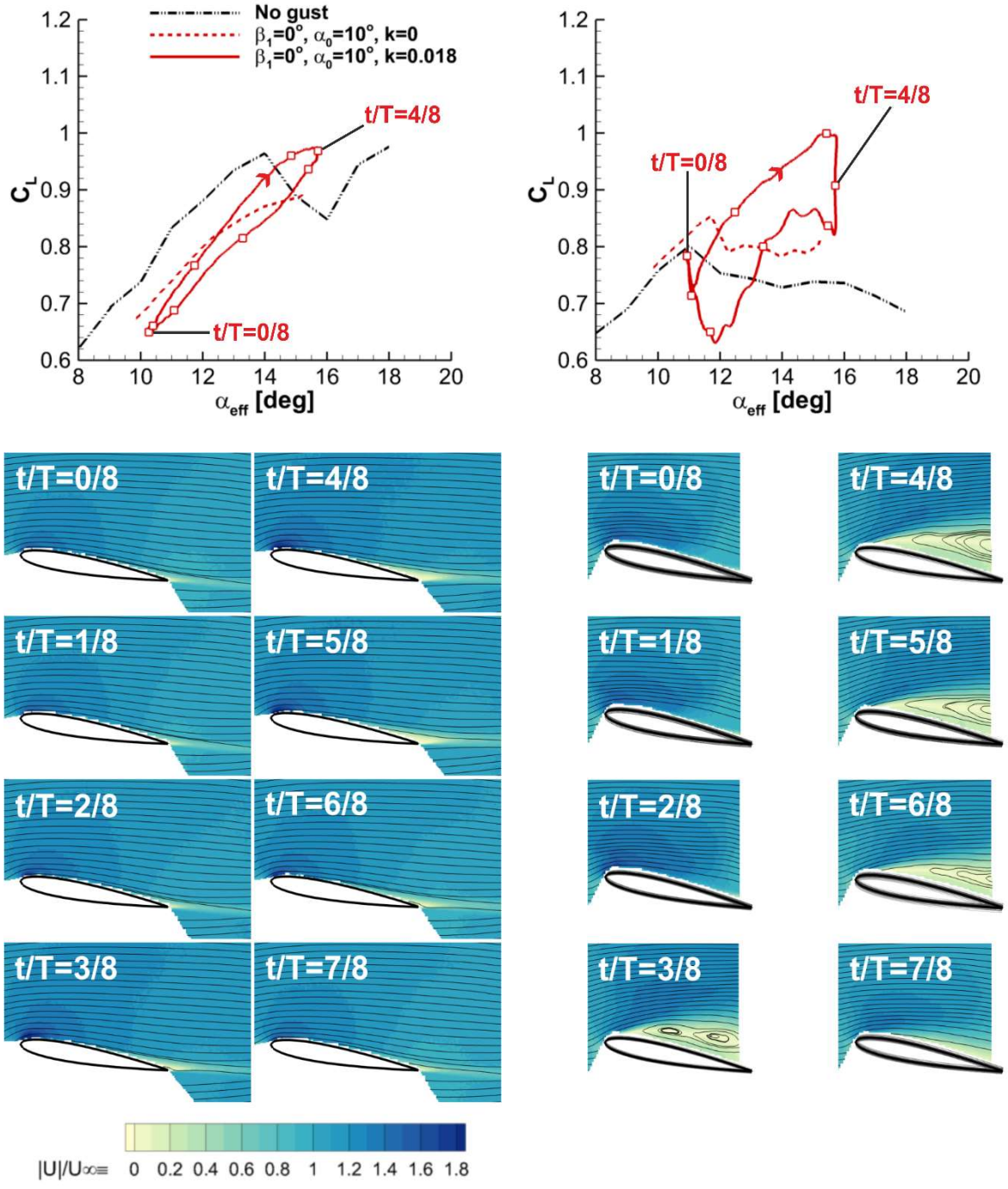

Figure 12: Loops of lift as a function of α_{eff} and accompanying PIV for the (a) low-flexibility and (b) high-flexibility wings at $\beta_1=0^o$, k=0.018, $\alpha_0=10^o$.

Figure 12 shows enlarged loops of aerodynamic C_L and accompanying phase-averaged PIV for both wings at α_0=10° for β_1=0°, k = 0.018. In the case of the low flexibility wing, shown in Figure 12a, PIV reveals nominally attached flow throughout the cycle. The velocity over the suction surface increases from its minimum at t/T=0/8 until its peak at t/T=4/8, in agreement with the location of the maximum lift coefficient $C_{L\,MAX}$. The boundary layer starts to thicken significantly at t/T=4/8 and is responsible for the reduced lift seen during the subsequent decline of α_{eff}, leading to clockwise hysteresis. On the high flexibility wing, shown in Figure 12b, flow separation at t/T=3/8 develops a region of recirculation centred over the suction surface which coincides with the maximum lift overshoot. Recirculating regions in phase-averaged PIV were associated with increased lift in Fernandez et al. (2021), while the vorticity fields are less coherent in the phase-averaged flow. By t/T=4/8 the recirculating region has thickened and the center has moved downstream, resulting in the stall of lift. Higher-frequency oscillations are noted during the decrease of α_{eff} due to excitation of the wing's bending and torsional modes which are reflected in the scatter of the wing profiles in the PIV averages.

Figure 13 shows similar data for the wings at higher angle of attack α_0=12° for β_1=0°, k = 0.018. As can be seen in Figure 13 a, the low flexibility wing maintains attached flow during the rise of α_{eff} until t/T=3/8, while C_L overshoots steady and baseline values. At t/T=3/8, the lift coefficient reaches its maximum and the boundary layer begins to separate from the trailing-edge. This is followed by lift stall at t/T=4/8, which is reflected in the drop of C_L at this phase and causes a relatively wide clockwise loop with hysteresis like that of the high flexibility wing at α_0=12°. Some influence of the wing's flexural and torsional vibration is visible between t/T=4/8 and 7/8 due to unsteadiness in the separated shear layer. Figure 13b shows that the high flexibility wing spends the whole cycle above the static stall angle of the baseline curve, in agreement with the separated flow seen throughout in PIV, though unsteady C_L is nonetheless able to overshoot the steady $C_{L\,MAX}$. The separated region is thinnest during the rise off α_{eff} from t/T=0/8 until t/T=3/8 and thickens substantially during its fall from t/T=4/8 to t/T=6/8, causing a narrow clockwise hysteresis loop. There is also significant high-frequency oscillations of the wing, represented here by the scatter in the location of the wing's cross section.

For the reduced frequency k = 0.072, Figure 14 shows the aeroelastic response of the wings for varying α_0 at β_1=0°. For the low flexibility wing, as shown in Figure 14a, the effective gust profile ($\alpha_{eff} - \alpha_0$) follows the gust profile closely with a slight positive shift for the higher α_0

which was also noted at the lower frequency. The inertial force is still small, and reveals oscillations at the second harmonic of the gust frequency (the natural bending frequency of this

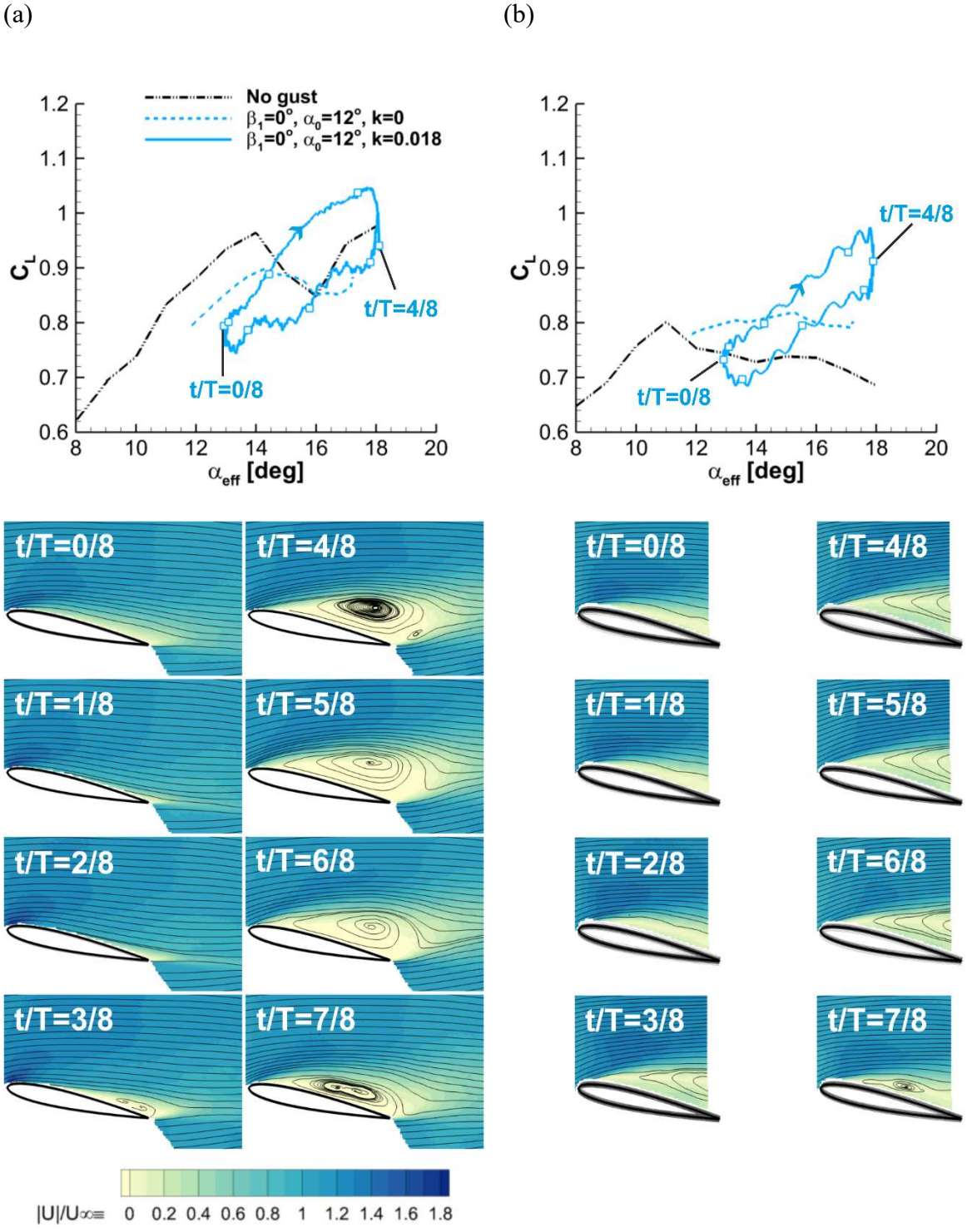

Figure 13: Loops of lift as a function of α_{eff} and accompanying PIV for the (a) low-flexibility and (b) high-flexibility wings at $\beta_1=0^o$, $k=0.018$, $\alpha_0=12^o$.

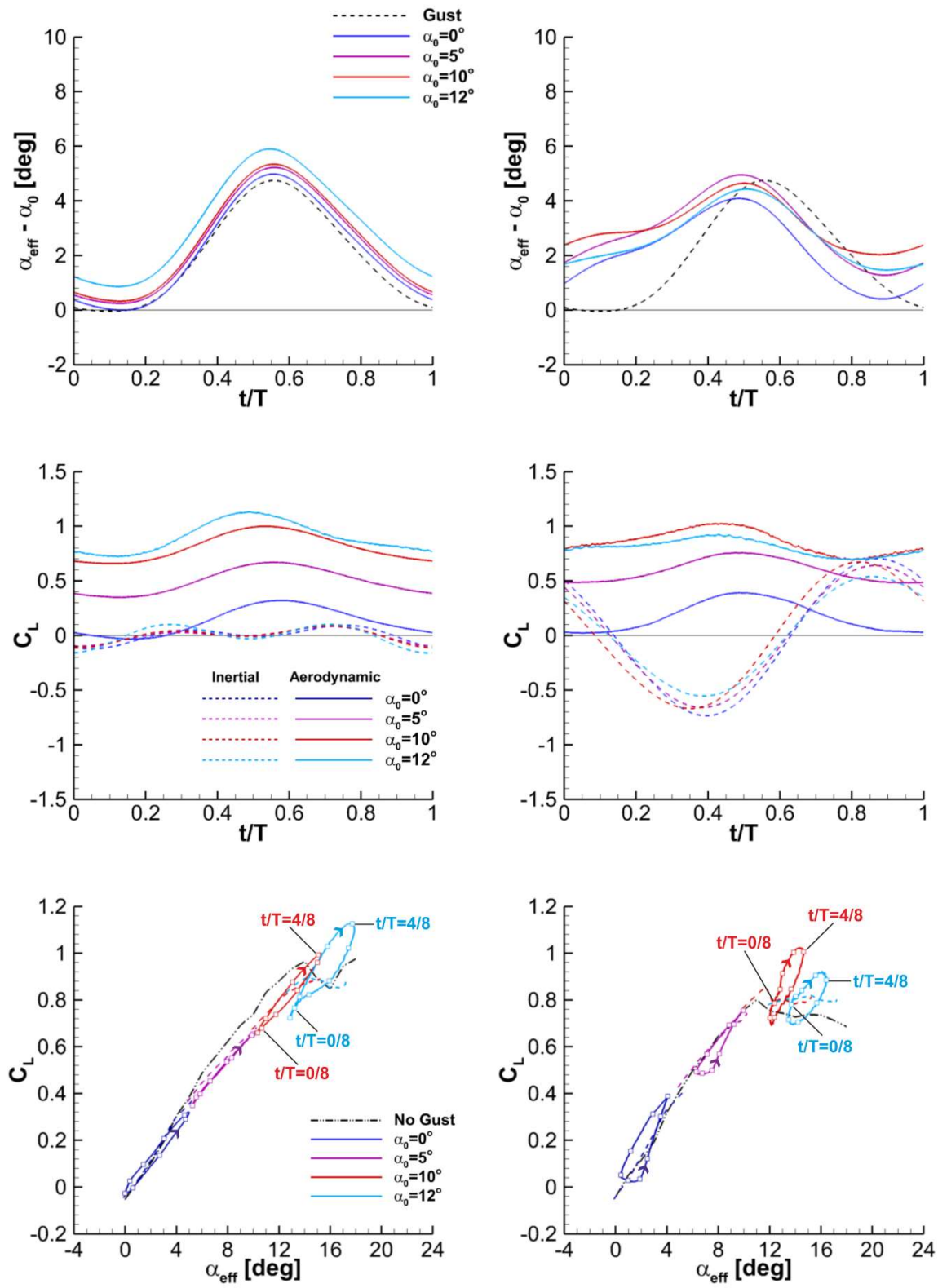

Figure 14: Comparison of effective gust angle, inertia force and aerodynamic lift for the (a) low-flexibility and (b) high-flexibility wings at β_1=0°, k=0.072.

wing is close to the second harmonic of the gust frequency). The features of $C_L = C_L$ (α_{eff}) loops are relatively unaffected when compared to the lower frequency for the same wing. In contrast, the high flexibility wing is in resonance and the ($\alpha_{eff} - \alpha_0$) profiles, shown in Figure 14b, reveal amplitude attenuation and phase angle relative to the gust profile, with little influence from α_0.

Comparison of inertial force and aerodynamic C_L shows that magnitudes are comparable, which cause large uncertainty in the lift coefficient in some parts of the cycle. The corresponding $C_L = C_L$ (α_{eff}) loops are plotted in Figure 14b to compare with the rigid wings and the flexible wings in non-resonant gusts (Fernandez et al. 2021; Fernandez 2021). It is seen that higher α_0 produce small clockwise loops with much less hysteresis than seen on rigid and non-resonating flexible wings. Thus, the aerodynamic C_L of the flexible wings at resonance could not be measured accurately, and will be disregarded in further analysis derived from the unsteady force measurements. The $C_L = C_L$ (α_{eff}) plots at resonance are included as a comparison only and also to discuss the PIV measurements and to reveal the range of α_{eff} (which is derived from the deformation measurements only).

Velocity measurements for the low flexibility wing are shown in Figure 15a at $\alpha_0 = 10^o$ for $\beta_1=0^o$, $k = 0.072$, along with $C_L = C_L$ (α_{eff}) loop. Flow is attached throughout, with peak velocity over the leading-edge at t/T=4/8 in agreement with the timing of $C_{L\,MAX}$. Thickening of the boundary layer is seen near the trailing edge from t/T=5/8 to t/T=6/8 which may be responsible for the slight clockwise hysteresis of the C_L loop. For the high flexibility wing, flow over the wing varies from weakly separated to fully separated at t/T=4/8, as shown in Figure 15b. Despite spending the entire cycle above the static stall angle, the flow approaches fully attached flow during the increase in the effective angle of attack.

Figure 16 shows the aeroelastic response of the wings for varying α_0 at $\beta_1=90^o$ and $k = 0.117$. Here it is the low flexibility wing that is in resonance, and the ($\alpha_{eff} - \alpha_0$) profiles in Figure 16a are flattened, as was previously observed for the high-flexibility wing at resonance. The inertial force curves are also in agreement with previous resonance cases, with magnitudes comparable to those of the aerodynamic C_L curves, and are nearly independent of α_0. The high flexibility wing, shown in Figure 16b, encounters gusts at $k > k_n$, so the plunging motion is reduced and the ($\alpha_{eff} - \alpha_0$) curves follow the gust in an orderly fashion. The inertial force component is reduced accordingly, and becomes smaller compared to the aerodynamic component. The $C_L = C_L$ (α_{eff}) loops remain consistent with those discussed previously: quasi-steady behaviour at $\alpha_0=0^o$ and 5°, and forms wider clockwise loops at higher α_0 due to aerodynamic stall. The

curves for the resonance cases in Figure 16a are plotted for comparison, however will be removed from further analysis due to their large uncertainty.

(a) (b)

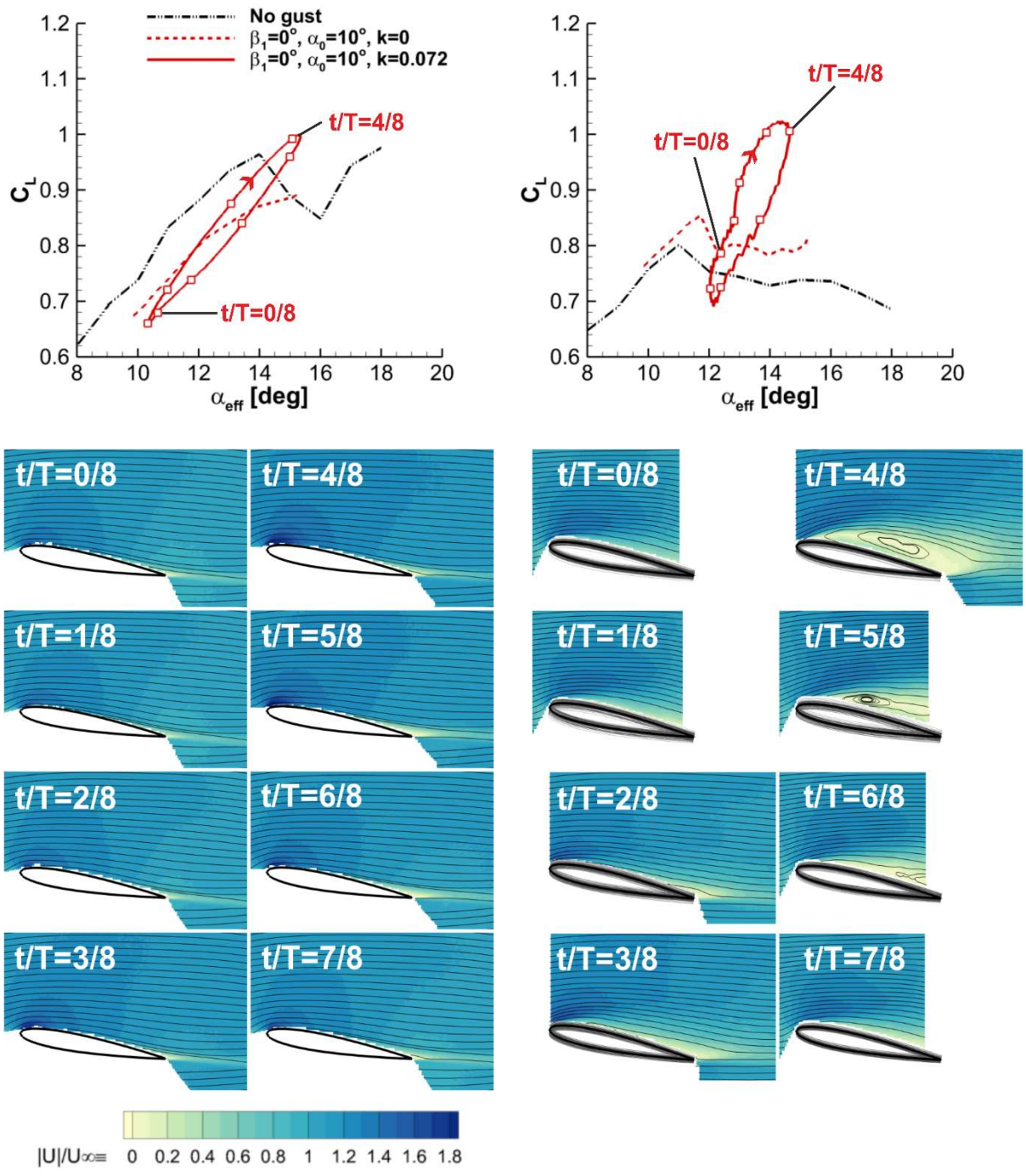

Figure 15: Loops of lift as a function of α_{eff} and accompanying PIV for the (a) low-flexibility and (b) high-flexibility wings at β_1=0°, k=0.072, α_0=10°.

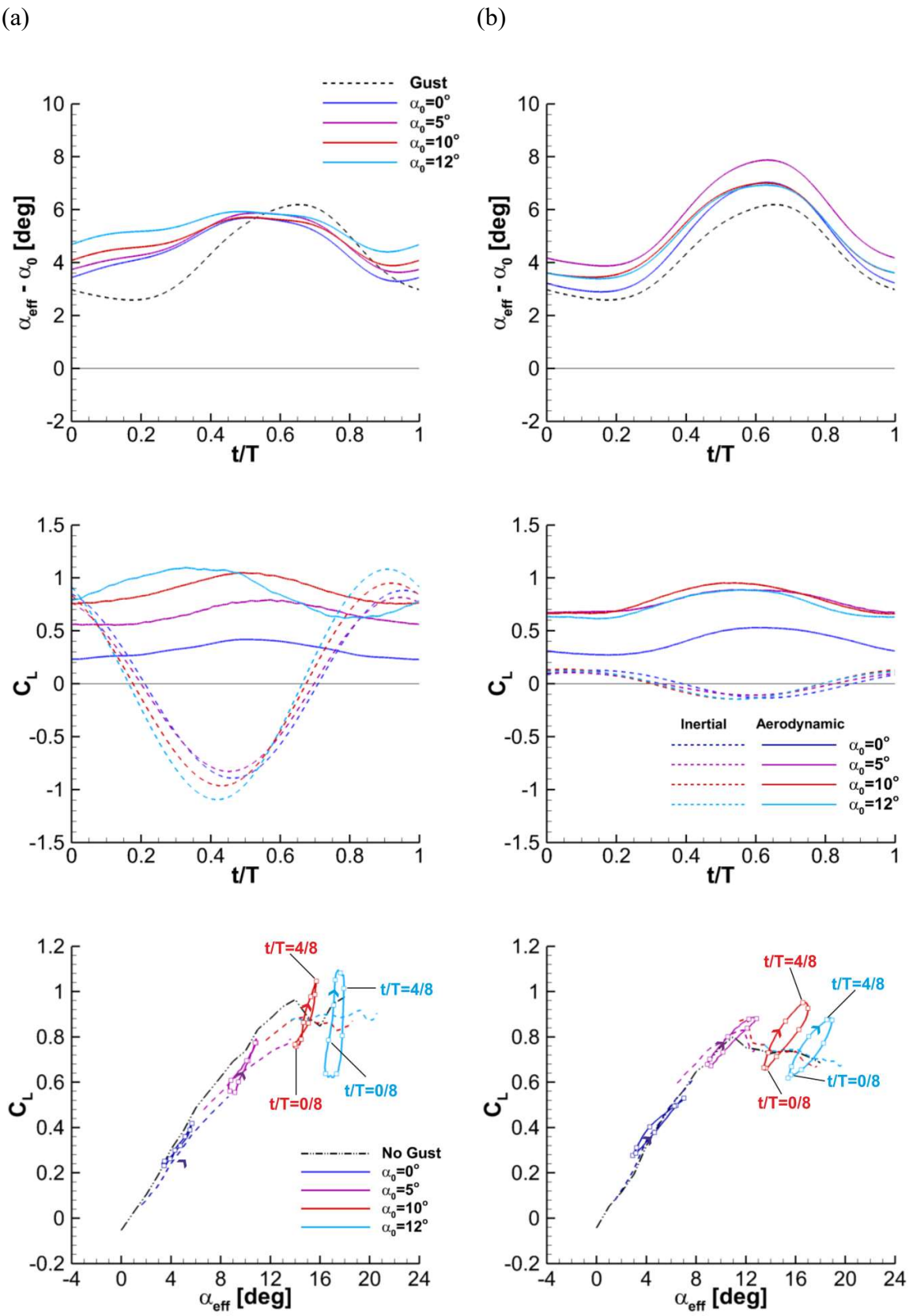

Figure 16: Comparison of effective gust angle, inertia force and aerodynamic lift for the (a) low-flexibility and (b) high-flexibility wings at β_1=90°, k=0.117.

Figure 17a shows PIV and accompanying lift coefficient for the low flexibility wing at α_0=10°. As the wing is in resonance the aerodynamic C_L must be disregarded, but the α_{eff} range (obtained from the deformation measurements) shows us that the wing remains above the static stall angle α_{ss} for the whole cycle. Despite this there is no evidence of aerodynamic stall, and flow remains attached throughout the whole cycle with some trailing-edge separation, as seen in Figure 15a. Figure 17b shows similar data for the high-flexibility wing, which remains well above α_{ss} for the entire cycle, resulting in separated flow throughout. The size of the separated region remains nearly constant as α_{eff} rises from t/T=0/8 to 4/8, accompanying a rise in C_L which overshoots the static $C_{L\,MAX}$. At t/T=6/8 the separated region increases and lift decreases. For this case, the wing's location varies substantially due to high-frequency wing vibrations.

For the largest reduced frequency k = 0.181, Figure 18 displays the aeroelastic response of the wings for varying α_0 at β_1=0°. Here, both wings are excited at $k > k_n$, and plunging motion is highly damped. For the low flexibility wing, shown in Figure 18a, the ($\alpha_{eff} - \alpha_0$) curves follow the gust closely with the expected positive shift with increasing α_0. The inertial force component is smaller than the aerodynamic component. The $C_L = C_L$ (α_{eff}) loops are consistent with those of the same wing at k = 0.072, as shown in Figure 14a, though the ($\alpha_{eff} - \alpha_0$) = 12° case exhibits lower hysteresis, similar to that of α_0=10°. The high-flexibility wing's behaviour, shown in Figure 18b, is practically the same as that of the low-flexibility wing. The loop for α_0 = 10° shows low hysteresis for a post-stall incidence.

The flow field around the low flexibility wing, shown in Figure 19a for k = 0.181 and α_0 = 10°, is fully attached and shows a peak in suction-side velocity at t/T=5/8, in agreement with C_{LMAX}, and a thicker wake during the decline of α_{eff} (from t/T=5/8 – 0/8) consistent with the slight clockwise hysteresis. The high flexibility wing, shown in Figure 19b for the same conditions, appears to have separated flow throughout. Although reduced hysteresis in the more separated flows may appear counter-initiative, similar cases were observed (Fernandez et al. 2021) when fully separated flow underwent small changes. In Figure 19b, it is apparent that the wake becomes larger when the effective angle of attack decreases.

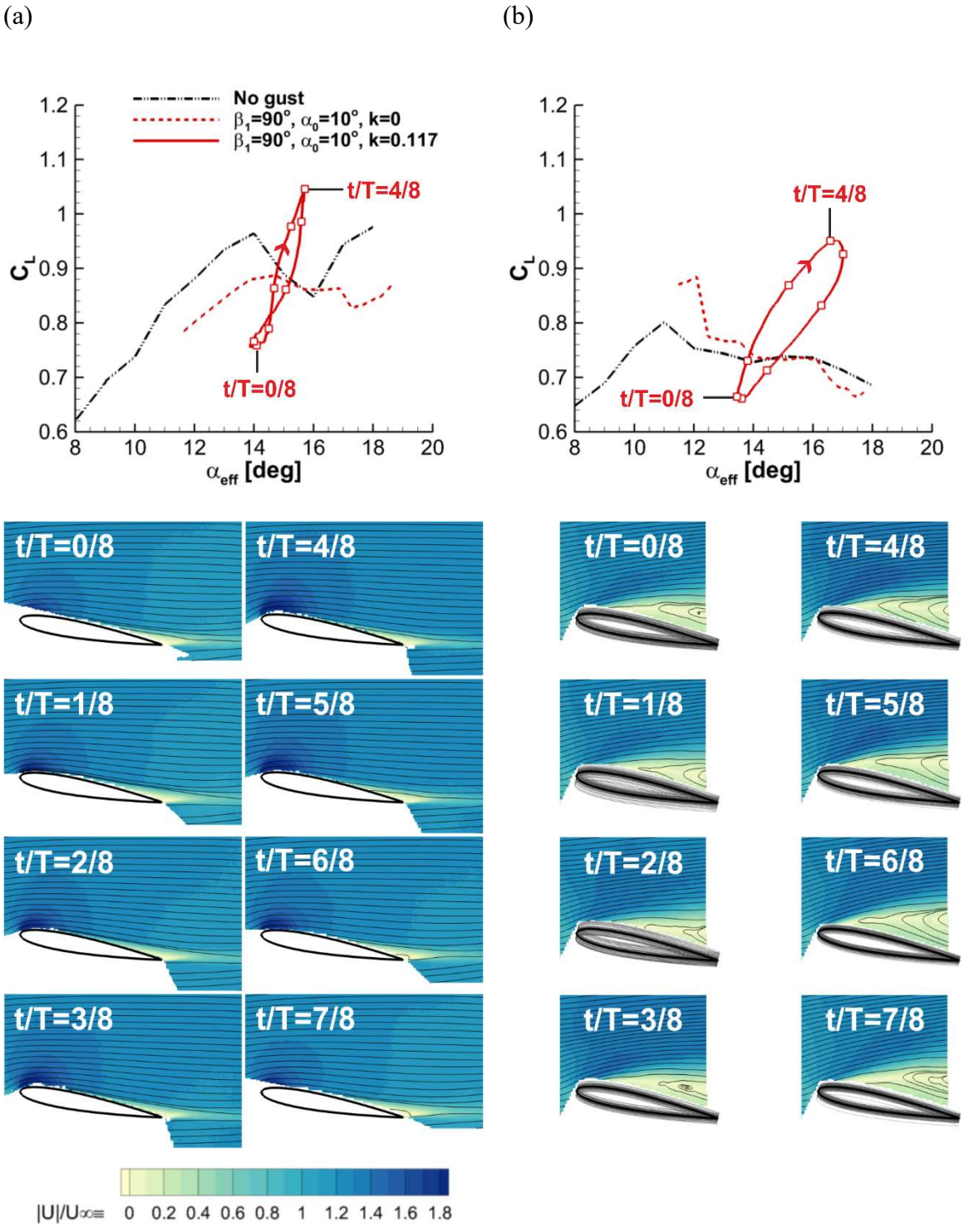

Figure 17: Loops of lift as a function of α_{eff} and accompanying PIV for the (a) low-flexibility and (b) high-flexibility wings at β_1=90°, k=0.117, α_0=10°.

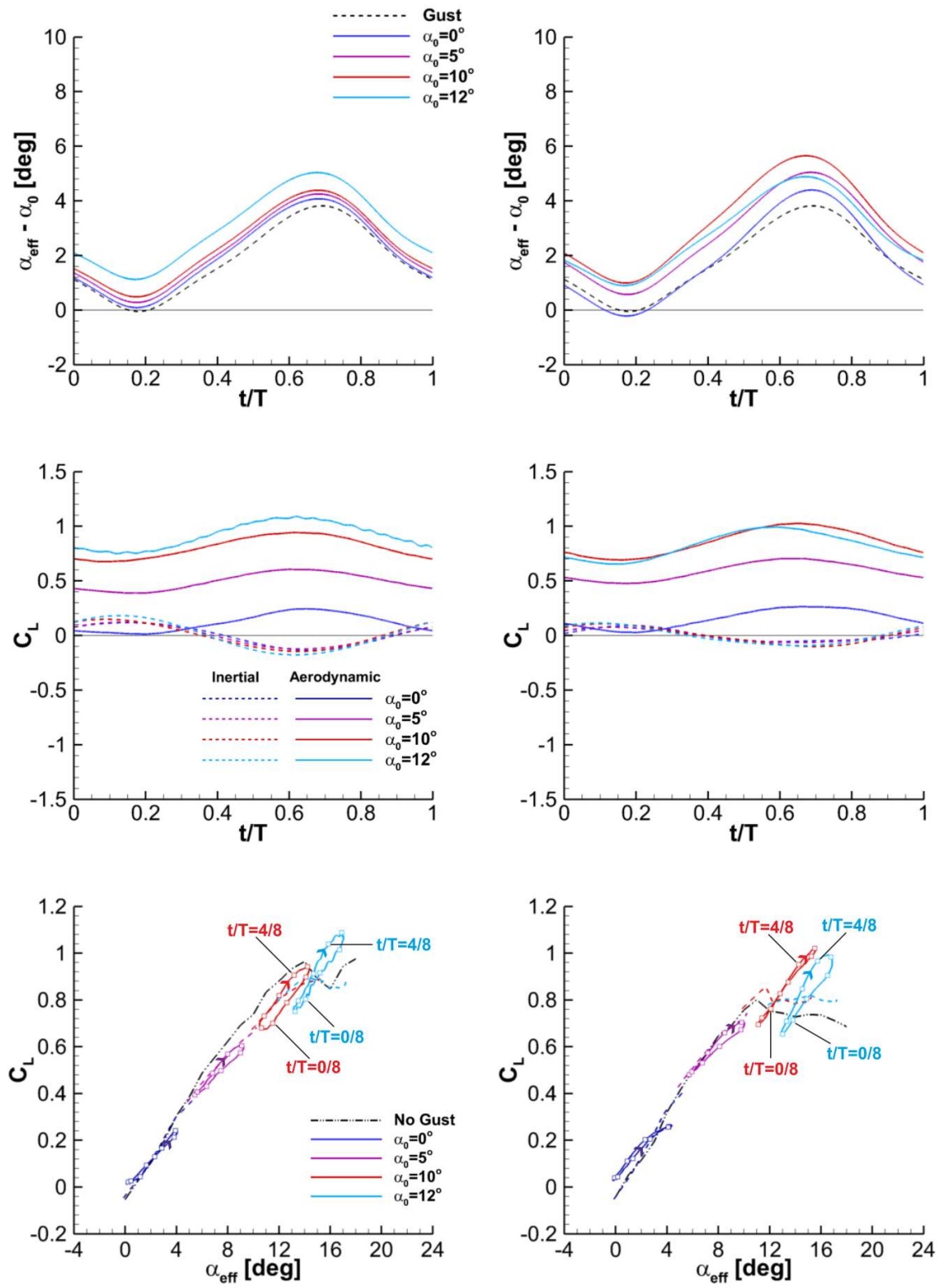

Figure 18: Comparison of effective gust angle, inertia force and aerodynamic lift for the (a) low-flexibility and (b) high-flexibility wings at β_1=0°, k=0.181.

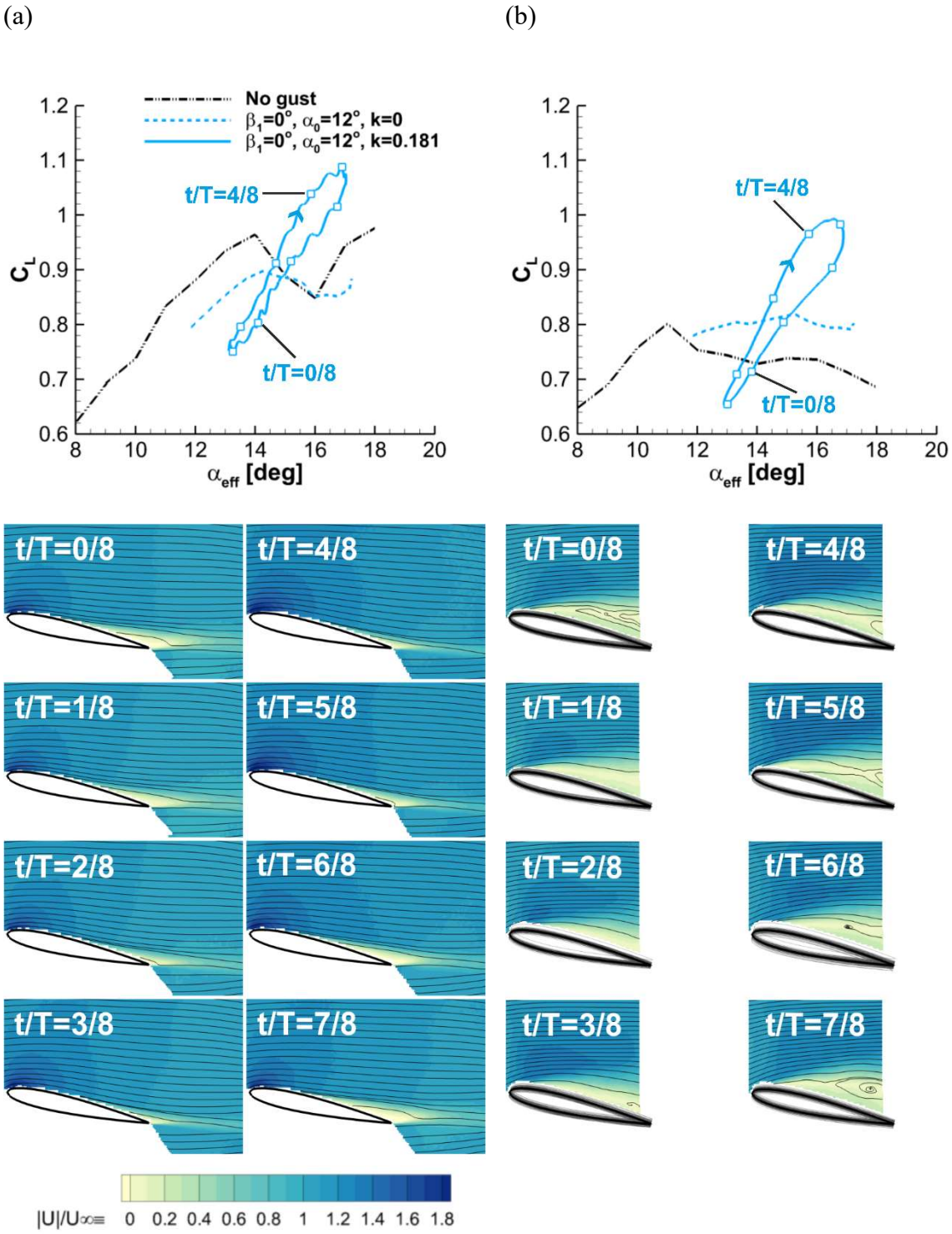

Figure 19: Loops of lift as a function of α_{eff} and accompanying PIV for the (a) low-flexibility and (b) high-flexibility wings at β_1=0°, k=0.181, α_0=12°.

E. Normalized Lift Response to Gusts

Figure 20a shows the normalized lift response of an equivalent rigid wing for the same range of k and α_0 studied (Fernandez et al. 2021). The lift response is defined as the peak-to-peak aerodynamic C_L amplitude normalized by the gust amplitude and static lift slope at $\alpha_{eff}=0^o$. No distinction is made between the different β_1 for the sake of clarity, and all gusts were included in this plot. A theoretical solution using Theodorsen's theory is also given, along with the bounds for the given frequency range. As explained in the original reference, the normalized response depends on the extent of stall. Attached flows produced near-theoretical lift response, but cases which penetrated stall reached significantly higher normalized amplitudes of up to 1.5 for $k > 0.017$. Figure 20b shows similar data for the flexible wings, with resonance cases omitted due to their large uncertainty. The lift amplitudes achieved for the flexible wings are evidently lower than those of the equivalent rigid wing, and only the highest k and α_0 of the low-flexibility wing approach the high amplitudes which appear throughout most of the k range for the rigid wing at $\alpha_0=10^o$ and 12^o.

Figure 21 shows the normalized lift response of the rigid and flexible wings on a single plot as a function of maximum effective angle of attack. This quantity appeared to be the most important parameter for the gust response of the rigid wings (Fernandez et al. 2021). In Figure 21 the data for the rigid, low-flexibility (LF) and high-flexibility (HF) wings were coloured according to the value of the reduced frequency k. The three wings seem to follow the same trend: as $max(\alpha_{eff})$ exceeds a critical value, the lift response is amplified at higher frequencies, but falls close to zero at lower k. The low flexibility wing undergoes greater amplification at high k than the high-flexibility wing, which is barely able to exceed a normalized amplitude of unity. Hence, wing flexibility is thought to directly damp the lift response to the gusts.

Figure 22 presents the steady and unsteady lift measurements at all α_0 and k – including the steady gusts as well as no gusts (steady freestream) – on a single plot for each wing. Resonance cases are omitted from the data of the flexible wings. All three wings are seen to follow similar, linear trends at low α_{eff}, but at a critical point near the static stall angle hysteresis becomes dominant. The low flexibility wing (Figure 22b) reaches this critical point at approximately $\alpha_{eff} = 12^o$, which is slightly higher than that of the rigid wing, which occurs at $\alpha_{eff} = 11.5^o$ (Fernandez et al. 2021). Furthermore, the low flexibility wing produces a much smaller hysteresis envelope. This is the direct evidence of decreasing lift response when subjected to the same gusts. Meanwhile the high flexibility wing – shown in Figure 22c – stalls earlier, as

aerodynamic forces twist the wing and increase its α_{eff}, and hysteresis dominates above α_{eff} = 11°. The high flexibility wing operates in deeper stall than the low flexibility wing, yet produces smaller hysteresis envelope.

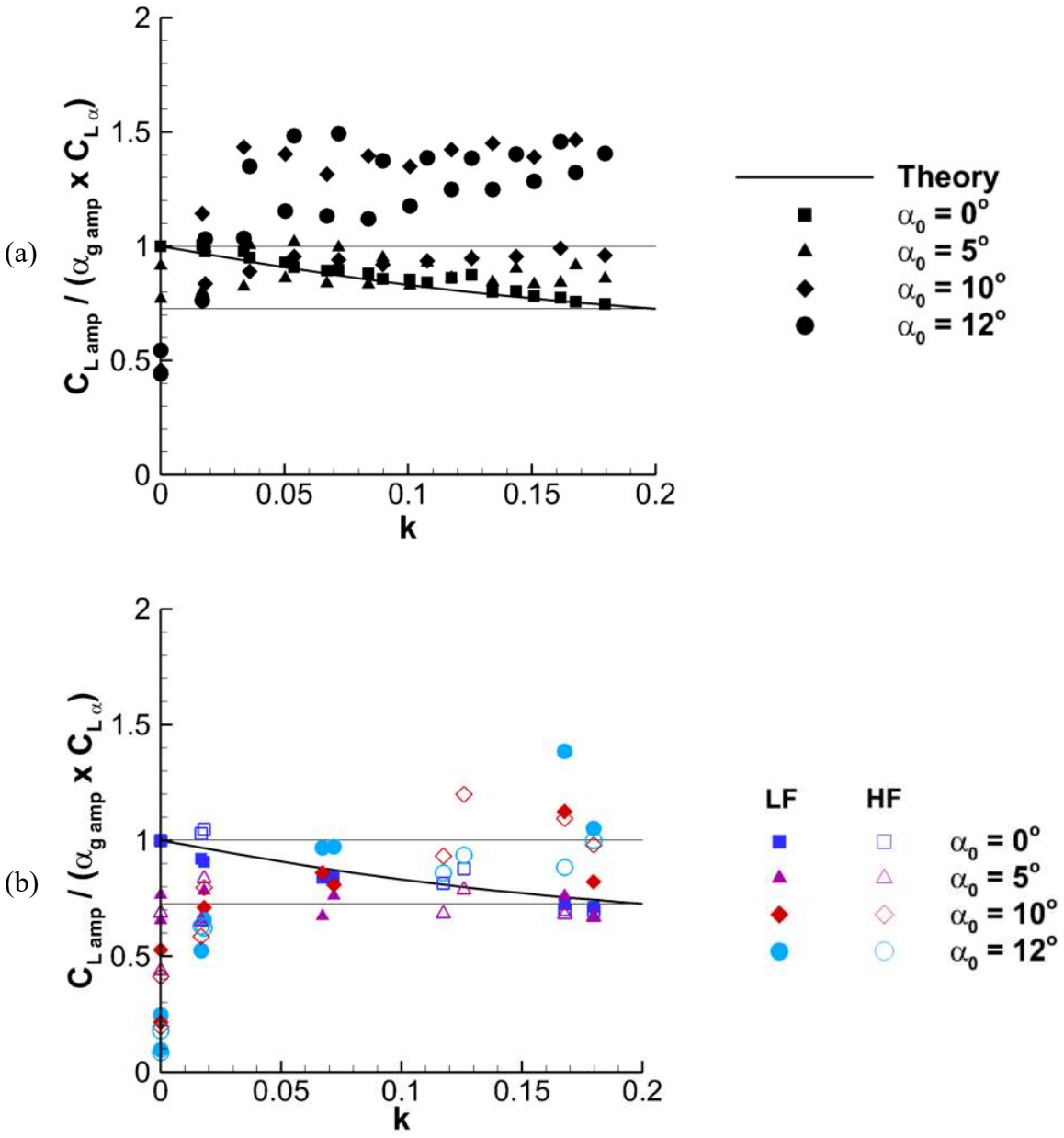

Figure 20: Normalised lift amplitude as a function of reduced frequency for the (a) rigid, (b) flexible wings. Horizontal lines denote the limits of the theoretical amplitude response at *k*=0 and 0.2.

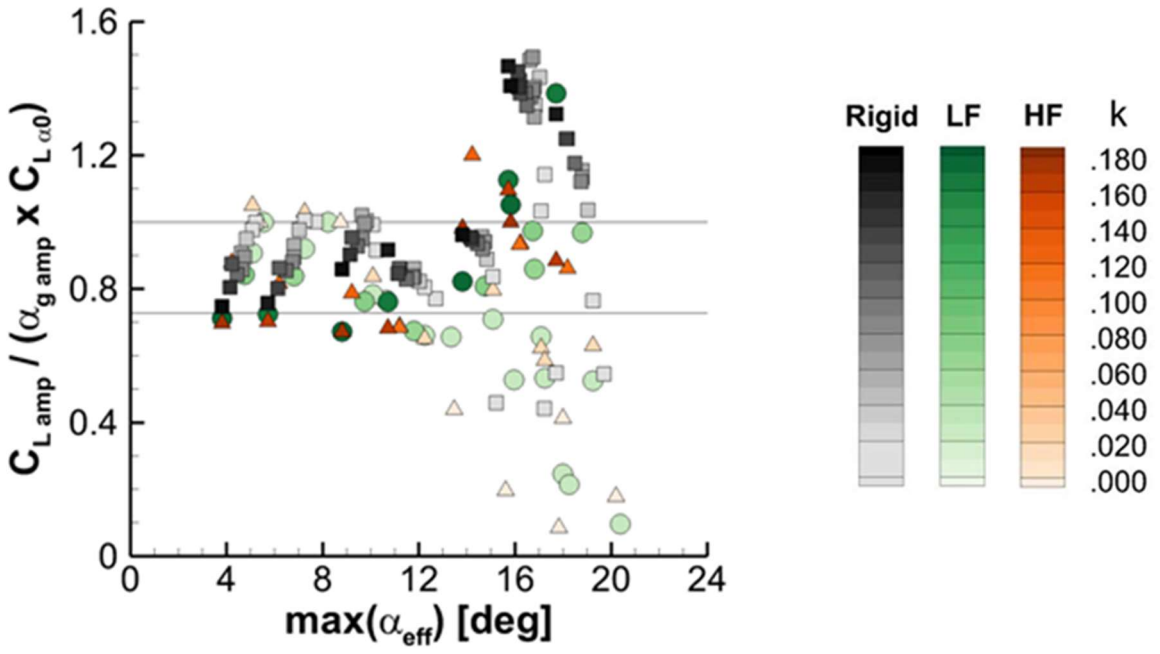

Figure 21: Normalised lift amplitude as a function of maximum effective angle of attack for rigid, low-flexibility and high-flexibility wings. Horizontal lines denote the limits of the theoretical amplitude response at k=0 and 0.2.

IV. Conclusions

Unsteady aerodynamics of flexible cantilevered wings in transverse gusts has been studied in wind tunnel experiments by means of force, velocity, and deformation measurements. Using a purpose-built gust generator, two flexible wings were subjected to small amplitude transverse gusts in a reduced frequency range of $k < 0.2$. The two flexible wings have been designed such that their first bending mode frequencies lie in the range of gust frequencies tested. The effective angle of attack, which is the sum of the geometric angle of attack at the root, twist angle, plunge angle due to the bending deflections, and the gust angle, was quantified as a function of gust reduced frequency. For both flexible wings, the effect of the bending deflections near the resonant frequency significantly counteracts the increase in the gust angle, reducing the effective angle of attack range. Away from the resonant frequency, the amplitude of the effective angle of attack does not differ much from the gust amplitude as the time-dependent deformation remains small. Hence, the wing flexibility attenuates the gust angle perceived by the wing.

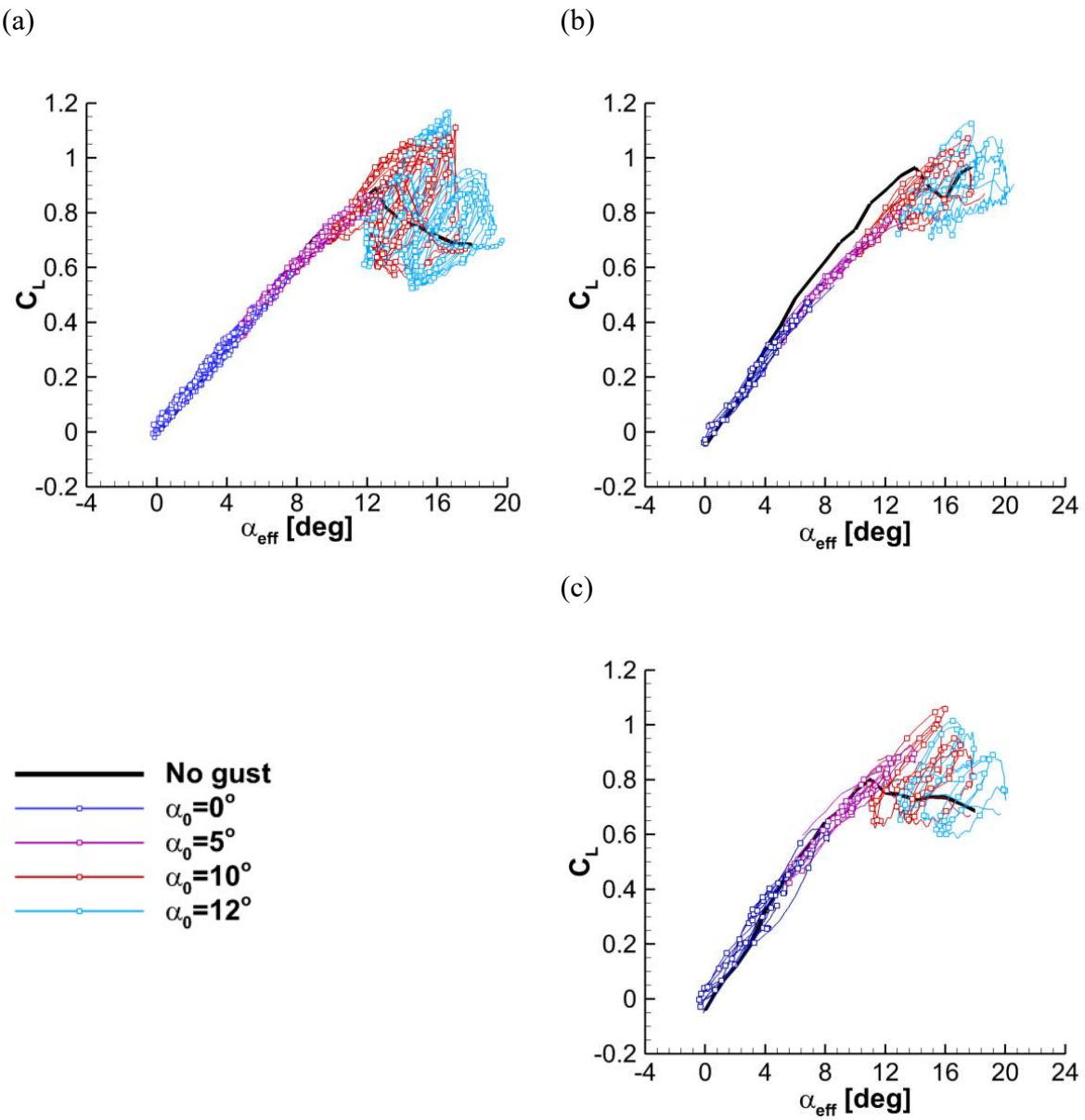

Figure 22: Baseline, steady and unsteady C_L for the (a) rigid, (b) low-flexibility and (c) high-flexibility wings.

With increasing wing flexibility, separated flow becomes more predominant during the cycle, while attached flow is prevalent for the less flexible wing. As the gust frequency increases, separated flow is seen through more of the cycle. At the resonant conditions, unsteady lift could not be measured accurately due to the large inertia force caused by the bending oscillations. However, even at resonant conditions, PIV measurements confirmed that attached flow may be maintained for the low flexibility wing. This is thought to be caused by the large bending oscillations (and plunge angle) decreasing the effective gust angle, which is confirmed by the deformation measurements. For both flexible wings, the lift amplitude normalized by the gust

amplitude is smaller compared to the rigid wings with separated flows. Similarly to the rigid wings, the most important parameter is the maximum effective angle of attack attained during the gust encounter for the flexible wings. When the maximum effective angle of attack is smaller than a critical value, the lift amplitude normalized by the gust amplitude is close to the predictions by the Theodorsen theory. Above the critical value of the maximum effective angle of attack, the normalized lift can be much smaller (at low k) or much larger (at high k).

Acknowledgements

The authors would like to acknowledge the EPSRC strategic equipment Grant (EP/K040391/1 and EP/M000559/1) that made the velocity measurements possible, and the James Dyson Foundation PhD Scholarship for Engineering.

References

Al-Battal, N.H., Cleaver, D.J. and Gursul, I., 2019. Unsteady actuation of counter-flowing wall jets for gust load attenuation. Aerospace Science and Technology, vol. 89, pp. 175-191

Barnes, C.J. and Visbal, M.R., 2018. Gust response of rigid and elastically mounted airfoils at a transitional Reynolds number. Aerospace Science and Technology, Vol. 74, pp. 112-119.

Chen, H. and Jaworski, J.W., 2020. Aeroelastic interactions and trajectory selection of vortex gusts impinging upon Joukowski airfoils. Journal of Fluids and Structures, Vol. 96, 103026.

Cleaver, D.J., Calderon, D.E., Wang, Z., and Gursul, I., 2016. Lift enhancement through flexibility of plunging wings at low Reynolds numbers. Journal of Fluids and Structures, Vol. 64, pp. 27-45.

Culler, E.C.E., Fagley, C., Seidel, J., McLaughlin, T.E., and John A.N. Farnsworth, J.A.N., 2017. Developing a reduced order model from structural kinematic measurements of a flexible finite span wing in stall flutter. Journal of Fluids and Structure, Vol. 71, pp. 56-69.

Dimitriadis, G., and Li, J., 2009. Bifurcation behavior of airfoil undergoing stall flutter oscillations in low-speed wind tunnel. AIAA J. 47 (11), 2577–2596.

Dowell, E.H., 2015. A Modern Course in Aeroelasticity, fifth ed. Springer.

Ekaterinaris, J., and Platzer, M., 1998. Computational Prediction of Airfoil Dynamic Stall. Progress in Aerospace Sciences, Vol. 33, Nos. 11-12, pp. 759–846.

Fagley, C., Seidel, J., and McLaughlin, T., 2016. Cyber-physical flexible wing for aeroelastic investigations of stall and classical flutter. Journal of Fluids and Structures, Vol. 67, pp. 34-47.

Fernandez, F., Cleaver, D. and Gursul, I. 2021. Unsteady aerodynamics of a wing in a novel small-amplitude transverse gust generator. Experiments in Fluids, 62:9

Fernandez, F., 2021. Aerodynamics of Wings in Unsteady Freestreams. PhD Thesis, University of Bath.

Gursul, I., 2004. Vortex flows on UAVs: Issues and challenges. The Aeronautical Journal, December, 597-610.

Gursul, I., Cleaver, D.J. and Wang, Z., 2014. Control of low Reynolds number flows by means of fluid–structure interactions. Progress in Aerospace Sciences, Vol. 64, pp. 17-55.

Heathcote, D. J., 2017. Aerodynamic Loads Alleviation Using Mini-Tabs. PhD Thesis, University of Bath.

Heathcote, D.J., Gursul, I. and Cleaver, D.J., 2020. Dynamic Deployment of a Minitab for Aerodynamic Load Control. Journal of Aircraft, vol. 57, pp. 41-61.

Holmes, D., 1973. Lift and Measurements in an Aerofoil in Unsteady Flow. Paper Number: 73-GT-41, ASME International Gas Turbine Conference and Products Show, April 8–12, Washington, DC, USA.

McCroskey, W. J., 1982. Unsteady Airfoils. Annual Review of Fluid Mechanics, Vol. 14, No. 1, pp. 285–311.

Neumann, J. and Mai, H., 2013. Gust response: Simulation of an aeroelastic experiment by a fluid–structure interaction method. Journal of Fluids and Structures, 38, 290 - 302.

Sears, W.R., 1941. Some Aspects of Non-Stationary Airfoil Theory and Its Practical Application. Journal of the Aeronautical Sciences, 8, 104.

Shyy, W., Aono, H., Chimakurthi, S.K., Trizila, P., Kang, C.-K., Cesnik, C.E.S., and Liu, H., 2010. Recent progress in flapping wing aerodynamics and aeroelasticity. Progress in Aerospace Sciences, Vol. 46, pp. 284-327.

Simmons, J. M. and Platzer, M.F. 1971. Experimental Investigation of Incompressible Flow Past Airfoils with Oscillating Jet Flaps. Journal of Aircraft, 8(8), 587–592.

Tang, D. and Dowell, E., 2001. Experimental and Theoretical Study on Aeroelastic Response of High-Aspect-Ratio Wings. AIAA Journal, Vol. 39, No. 8, pp. 1430-1441.

Tang, D., Grasch, A. and Dowell, E.H., 2010. Gust Response for Flexibly Suspended High-Aspect Ratio Wings. AIAA Journal, Vol. 48, No. 10, pp. 2430-2444.

Taylor, G., Wang, Z., Vardaki, E. and Gursul, I., 2007. Lift Enhancement over Flexible Nonslender Delta Wings. AIAA Journal, Vol. 45, No. 12, pp. 2979-2993.

Theodorsen, T., 1935. General Theory of Aerodynamic Instability and the Mechanism of Flutter. N.A.C.A. Tech. Report No. 496, Washington, D. C.

Thorby, D. 2008. Structural Dynamics and Vibration in Practice. Elsevier.

von Karman, T. H., and Sears, W.R., 1938. Airfoil Theory for Non-Uniform Motion. Journal of the Aeronautical Sciences, Vol. 5, No. 10, Aug. pp. 379–390.

Wilder, M., & Telionis, D. 1998. Parallel Blade-Vortex Interaction. Journal of Fluids and Structures, 801-838.